



A Noninteracting Galactic Black Hole Candidate in a Binary System with a Main-sequence Star

Sukanya Chakrabarti¹, Joshua D. Simon², Peter A. Craig³, Henrique Reggiani², Timothy D. Brandt⁴,
Puragra Guhathakurta⁵, Paul A. Dalba^{6,7,13}, Evan N. Kirby⁸, Philip Chang⁹, Daniel R. Hey¹⁰, Alessandro Savino¹¹,
Marla Geha¹², and Ian B. Thompson²

¹ Department of Physics and Astronomy, University of Alabama, Huntsville, 301 North Sparkman Drive, Huntsville, USA; sc0236@uah.edu

² Observatories of the Carnegie Institution for Science, 813 Santa Barbara Street, Pasadena, CA 91101, USA

³ School of Physics and Astronomy, Rochester Institute of Technology, 1 Lomb Memorial Drive, Rochester, NY 14623, USA

⁴ Department of Physics, University of California, Santa Barbara, Santa Barbara, CA 93106, USA

⁵ University of California Santa Cruz, UCO/Lick Observatory, 1156 High Street, Santa Cruz, CA 95064, USA

⁶ Department of Astronomy and Astrophysics, University of California, Santa Cruz, CA 95064, USA

⁷ SETI Institute, Carl Sagan Center, 339 Bernardo Avenue, Suite 200, Mountain View, CA 94043, USA

⁸ Department of Physics and Astronomy, University of Notre Dame, 225 Nieuwland Science Hall, Notre Dame, IN 46556, USA

⁹ Department of Physics, University of Wisconsin-Milwaukee, 3135 North Maryland Avenue, Milwaukee, WI 53211, USA

¹⁰ Institute for Astronomy, University of Hawai'i, Honolulu, HI 96822, USA

¹¹ Department of Astronomy, University of California, Berkeley, Berkeley, CA, 94720, USA

¹² Department of Astronomy, Yale University, 52 Hillhouse Avenue, New Haven, CT 06520, USA

Received 2022 October 12; revised 2023 March 8; accepted 2023 March 21; published 2023 June 8

Abstract

We describe the discovery of a solar neighborhood ($d = 468$ pc) binary system with a main-sequence sunlike star and a massive noninteracting black hole candidate. The spectral energy distribution of the visible star is described by a single stellar model. We derive stellar parameters from a high signal-to-noise Magellan/MIKE spectrum, classifying the star as a main-sequence star with $T_{\text{eff}} = 5972$ K, $\log g = 4.54$, and $M = 0.91 M_{\odot}$. The spectrum shows no indication of a second luminous component. To determine the spectroscopic orbit of the binary, we measured the radial velocities of this system with the Automated Planet Finder, Magellan, and Keck over four months. We show that the velocity data are consistent with the Gaia astrometric orbit and provide independent evidence for a massive dark companion. From a combined fit of our spectroscopic data and the astrometry, we derive a companion mass of $11.39^{+1.51}_{-1.31} M_{\odot}$. We conclude that this binary system harbors a massive black hole on an eccentric ($e = 0.46 \pm 0.02$), 185.4 ± 0.1 day orbit. These conclusions are independent of El-Badry et al., who recently reported the discovery of the same system. A joint fit to all available data yields a comparable period solution but a lower companion mass of $9.32^{+0.22}_{-0.21} M_{\odot}$. Radial velocity fits to all available data produce a unimodal solution for the period that is not possible with either data set alone. The combination of both data sets yields the most accurate orbit currently available.

Unified Astronomy Thesaurus concepts: Binary stars (154); Astrometric binary stars (79); Black holes (162); High-resolution spectroscopy (2096); Gaia (2360); Milky Way Galaxy (1054)

Supporting material: machine-readable table

1. Introduction

Simple stellar population calculations suggest that stellar mass black holes should be abundant (e.g., Breivik et al. 2017; Wiktorowicz et al. 2019), with $\sim 10^8$ present in the Milky Way (e.g., Olejak et al. 2020). However, black holes in this mass range are difficult to identify observationally. Isolated black holes can only be detected with gravitational microlensing (e.g., Lam et al. 2022; Sahu et al. 2022), while black holes in binary systems are only easily detectable when the companion star is close enough for an accretion disk to form. Although dozens of X-ray binaries with black hole candidates in short-period orbits have been identified (e.g., Corral-Santana et al. 2013, 2016; Panizo-Espinar et al. 2022; Russell et al. 2022), wider binaries have proven challenging to find.

The detection of gravitational waves from black hole merger events with LIGO (e.g., Abbott et al. 2016, 2019, 2021) has provided a new avenue for discovering binary black holes beyond the X-ray bright population (Corral-Santana et al. 2016). However, like the X-ray binaries, LIGO black hole mergers are necessarily found in very tight orbits. With the publication of the large catalog of binary systems included in the third Gaia data release (DR3; Gaia Collaboration et al. 2016, 2022a, 2022b; Halbwachs et al. 2022) and the anticipated even larger data set to come in fourth Gaia data release (DR4), we can expect to significantly expand upon discoveries of black holes in binary systems, and particularly for black holes in long-period systems that can be characterized by measuring accelerations from astrometric and spectroscopic data (e.g., Breivik et al. 2017; Mashian & Loeb 2017; Yamaguchi et al. 2018; Wiktorowicz et al. 2020; Chawla et al. 2022; Janssens et al. 2022). Since binaries are coeval, studying these systems may help in understanding the dependence of the formation rate of black holes in binaries on metallicity and age, and thereby indirectly on the formation channel.

¹³ Heising-Simons 51 Pegasi b Postdoctoral Fellow.

Several mechanisms for the formation of black holes in binary systems have been discussed in the literature. Binary black holes may form via common envelope evolution (Belczynski et al. 2016), stable mass transfer (van den Heuvel et al. 2017; Neijssel et al. 2019; Bavera et al. 2020; Marchant et al. 2021), chemically homogeneous evolution (de Mink & Mandel 2016), and dynamical processes in dense stellar environments (Antonini & Rasio 2016). Early studies of massive LIGO black holes attributed the formation of these systems to pristine low-metallicity environments, which may be found in dwarf galaxies or massive galaxies at high redshift (Lamberts et al. 2016). Another possibility is that these massive black holes may form in the outer HI disks of spiral galaxies (Chakrabarti et al. 2017, 2018), where low metallicities are also prevalent (e.g., Kennicutt & Bresolin 2003; Bresolin et al. 2012; Berg et al. 2020). Studies of the black hole–main-sequence (BH–MS) binary population discovered from Gaia can now reveal potential differences with respect to the black hole–black hole (BH–BH) and black hole–neutron star (BH–NS) demographics. Although it is now clear that there is a strong observed anticorrelation between metallicity and the close (periods $<10^4$ day) binary fraction for solar type stars (Gao et al. 2014; Moe et al. 2019), the reverse trend is apparent for the high-mass X-ray binary population (Lehmer et al. 2021).

Searches for noninteracting black holes in binary systems with luminous companions have intensified in recent years, with a number of claimed detections (e.g., Liu et al. 2019; Rivinius et al. 2020; Jayasinghe et al. 2021; Lennon et al. 2021; Jayasinghe et al. 2022; Saracino et al. 2022). However, most of these systems have been rapidly disputed or ruled out (e.g., Abdul-Masih et al. 2020; Bodensteiner et al. 2020; El-Badry & Quataert 2020; Eldridge et al. 2020; Shenar et al. 2020; El-Badry & Quataert 2021; El-Badry et al. 2022a, 2022c; El-Badry & Burdge 2022; Frost et al. 2022). To date, only a few likely black holes¹⁴ have survived this community vetting: a $>3 M_{\odot}$ black hole with a red giant companion (Thompson et al. 2019, although see van den Heuvel & Tauris 2020), a $>9 M_{\odot}$ black hole orbiting a massive O star in the Large Magellanic Cloud (Shenar et al. 2022), and a $>7 M_{\odot}$ black hole candidate orbiting the Galactic O star HD 130298 (Mahy et al. 2022). The object that we discuss in this paper has also been studied earlier by El-Badry et al. (2023b).

In work that is contemporaneous with ours (posted to the archive on 2022 September 14), El-Badry et al. (2023b) reported the independent discovery and analysis of the same source. Here, we present our independent analysis of a main-sequence G star on an eccentric 185 day orbit around a $\sim 10 M_{\odot}$ dark companion, which we selected from the Gaia DR3 binary catalog. Given the now available data published from El-Badry et al. (2023b), we also present RV-only fits to the combined data set (ours and that of El-Badry et al. 2023b), as well as joint fits that incorporate both sets of RV data and the astrometry.

Our search for black hole candidates in binary systems with luminous companions begins with the Gaia DR3 catalog of binary masses. Gaia DR3 provides the largest sample of binary stars that has been produced by the astronomical community thus far, yielding orbital solutions derived from astrometry and/or spectroscopy for $\sim 3 \times 10^5$ stars (Gaia Collaboration et al. 2022a; Halbwachs et al. 2022; Holl et al. 2022).

This paper is organized as follows. In Section 2, we briefly review our methodology, including our selection from the Gaia DR3 binary mass catalog, and additional tests. We provide all available photometry for the visible star, and describe our follow-up spectroscopic observations over the last several months and our procedures for measuring radial velocities. In Section 3, we describe our analysis of the observed spectral energy distribution (SED), fitting the photometric data with single source and multiple source models to find that the visible star is adequately described by a single stellar photosphere. In Section 4, we discuss the Gaia astrometric orbital solution and compute orbits from our velocity data alone, and from the combination of the velocities and the astrometry. We discuss our results in Section 5 and conclude in Section 6.

2. Methods and Data Collection

The Gaia DR3 non_single_stars catalog contains 195,315 binary systems with lower limits on the mass of the secondary star. From this set, we selected those for which the secondary was constrained to be more massive than the primary and at least $5 M_{\odot}$, which is well above the mass range of white dwarfs and neutron stars. We removed double-lined spectroscopic binaries and focused on bright ($G < 14$) companions that would allow for follow-up observations on a wide range of telescopes. For spectroscopic solutions, we retained sources that have at least 10 RV points as reported by Gaia and significance > 5 . As an Astronomical Data Query Language search, this selection is given by

```
select * from
gaiadr3.gaia_source inner join
gaiadr3.nss_two_body_orbit
using (source_id) inner join
gaiadr3.binary_masses
using (source_id)
where
m2_lower > 5 and
nss_solution_type != 'SB2' and
phot_g_mean_mag < 14 and
rv_nb_transits > 10 and
significance > 5
```

In addition, we required that sources lie within ~ 0.5 mag of the Gaia main sequence. Sources with spectral energy distributions (SEDs) that are well-described by a single star and are located on the main sequence are strong candidates for hosting dark companions because a luminous star that is more massive than the primary should be easily detectable (e.g., El-Badry & Rix 2022). Finally, we excluded sources that show variability in their TESS light curve, which would indicate that they are eclipsing binaries. These cuts left us with a set of sources on which we obtained follow-up RV measurements (to be discussed elsewhere).

In the remainder of this paper, we describe our results and analysis of one star, Gaia DR3 4373465352415301632, for which an astrometric orbit was reported in DR3. We display the position of this object in the Gaia color–magnitude diagram in Figure 1. In the DR3 binary catalog, Gaia DR3 4373465352415301632 has a primary¹⁵ mass of $0.95 M_{\odot}$, a secondary mass of $12.8_{-2.3}^{+2.8} M_{\odot}$, a

¹⁴ Here we set aside several black hole binary candidates in globular clusters (Giesers et al. 2018, 2019), which may have different formation mechanisms.

¹⁵ For this paper, we adopt the Gaia convention of referring to the luminous star as the primary and the nonluminous companion as the secondary, even though the latter may be more massive.

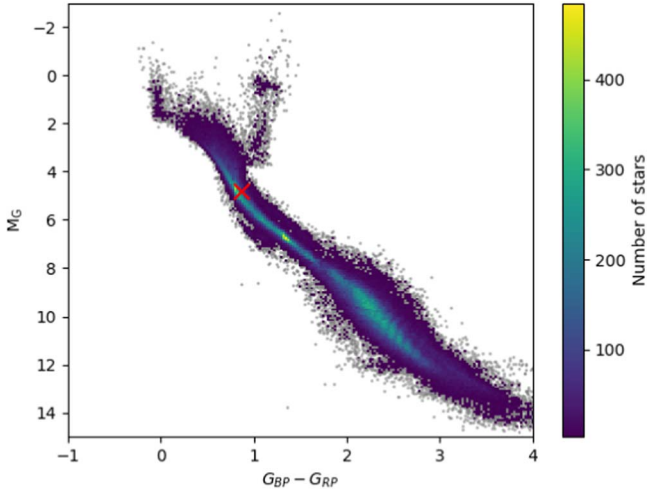


Figure 1. Gaia color–magnitude diagram. The extinction-corrected absolute magnitude and color of Gaia DR3 4373465352415301632, based on the Gaia parallax and G -band extinction, are marked with a red cross; the Gaia main sequence is apparent.

period of 185.8 ± 0.3 day, and an eccentricity of 0.49 ± 0.07 . However, the only radial velocity information provided by Gaia is a single measurement of $v = 23.0 \pm 2.6$ km s $^{-1}$. No spectroscopic orbital solution is included in DR3, which indicates that a spectroscopic orbit could not be determined from the 13 independent radial velocity measurements obtained by Gaia. Because the astrometric orbit is at the extreme edge of the distribution of companion masses in the DR3 catalog, the lack of spectroscopic confirmation raises the concern that the astrometric solution, and the parameters derived from it, could be erroneous (Gaia Collaboration et al. 2022a; Halbwachs et al. 2022). In this paper, we focus on this source because it is the most compelling black hole candidate (meeting our criteria above) for which we have obtained RV data thus far. Although spectroscopic observations for a limited number of other possible candidates are ongoing, analysis of these objects is beyond the scope of this paper.

We note that, in addition to the comprehensive analysis by El-Badry et al. (2023b), two other recent studies of the DR3 data set have also discussed this star as a candidate black hole binary. Andrews et al. (2022) selected 24 candidate compact object binaries from the DR3 astrometric orbital solutions and obtained follow-up spectroscopy of some of them, including Gaia DR3 4373465352415301632. However, they discarded it because the orbital period is close to an integer multiple of the Gaia scanning law, which suggests that the derived orbit could be an artifact. Shahaf et al. (2023) used the astrometric mass ratio function to identify 177 candidate binaries containing compact objects. In their sample, Gaia DR3 4373465352415301632 has the highest secondary mass of the Class III sources, for which a compact object is the only viable type of companion, but no follow-up observations were obtained.

2.1. Photometry

We retrieved UV-IR photometry for this source from GALEX (Martin et al. 2005), SDSS (Fukugita et al. 1996), the APASS survey (Henden et al. 2016), Gaia DR3 (Riello et al. 2021), PanSTARRS (Tonry et al. 2012), SkyMapper (Wolf et al. 2018), 2MASS (Skrutskie et al. 2006), and WISE (Wright et al. 2010). Figure 2 displays the available photometry

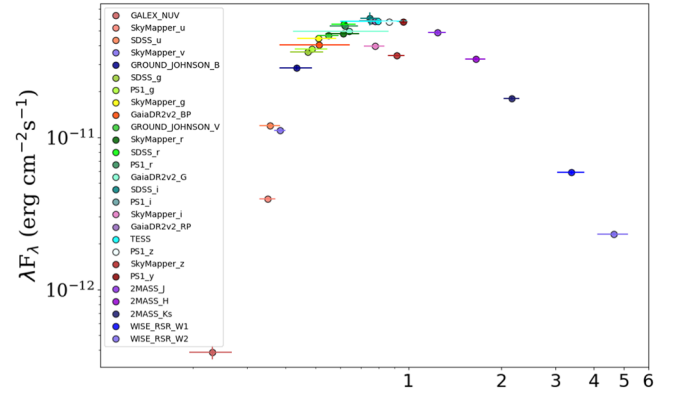


Figure 2. Available photometry of Gaia DR3 4373465352415301632 from the near-UV to the mid-infrared, with the data sources given in the legend.

Table 1
Photometry for Gaia DR3 4373465352415301632

Survey	Band	Magnitude	Magnitude Uncertainty
GALEX	<i>NUV</i>	20.281	0.115
SDSS	<i>u</i>	16.026	0.006
SDSS	<i>g</i>	14.504	0.003
SDSS	<i>r</i>	13.768	0.003
SDSS	<i>i</i>	13.462	0.004
SDSS	<i>z</i>	13.308	0.004
APASS	<i>B</i>	14.971	0.088
APASS	<i>V</i>	14.091	0.045
GaiaDR3	<i>BP</i> ^a	14.276	0.001
GaiaDR3	<i>G</i> ^a	13.772	0.001
GaiaDR3	<i>RP</i> ^a	13.101	0.001
Pan-STARRS	<i>g</i>	14.420	0.002
Pan-STARRS	<i>r</i>	13.781	0.002
Pan-STARRS	<i>i</i>	13.479	0.001
Pan-STARRS	<i>z</i>	13.346	0.002
Pan-STARRS	<i>y</i>	13.242	0.001
SkyMapper	<i>u</i>	16.041	0.010
SkyMapper	<i>v</i>	15.654	0.008
SkyMapper	<i>g</i>	14.252	0.005
SkyMapper	<i>r</i>	13.786	0.005
SkyMapper	<i>i</i>	13.450	0.004
SkyMapper	<i>z</i>	13.303	0.004
2MASS	<i>J</i>	12.244	0.024
2MASS	<i>H</i>	11.895	0.023
2MASS	<i>Ks</i>	11.780	0.023
WISE	<i>W1</i>	11.691	0.023
WISE	<i>W2</i>	11.717	0.022
WISE	<i>W3</i>	11.671	0.232

Note.

^a The formal uncertainties on the Gaia DR3 photometry are smaller than listed here but are rounded to 1 mmag for convenience and because calibration errors between surveys will limit cross-survey comparisons to a coarser level.

for this source, and Table 1 lists the measurements and associated errors in each band. We analyze the spectral energy distribution of this source later on and discuss our choice of photometry.

2.2. Spectroscopy

2.2.1. Observations and Data Reduction

We obtained follow-up high-resolution spectroscopy of Gaia DR3 4373465352415301632 to determine its stellar

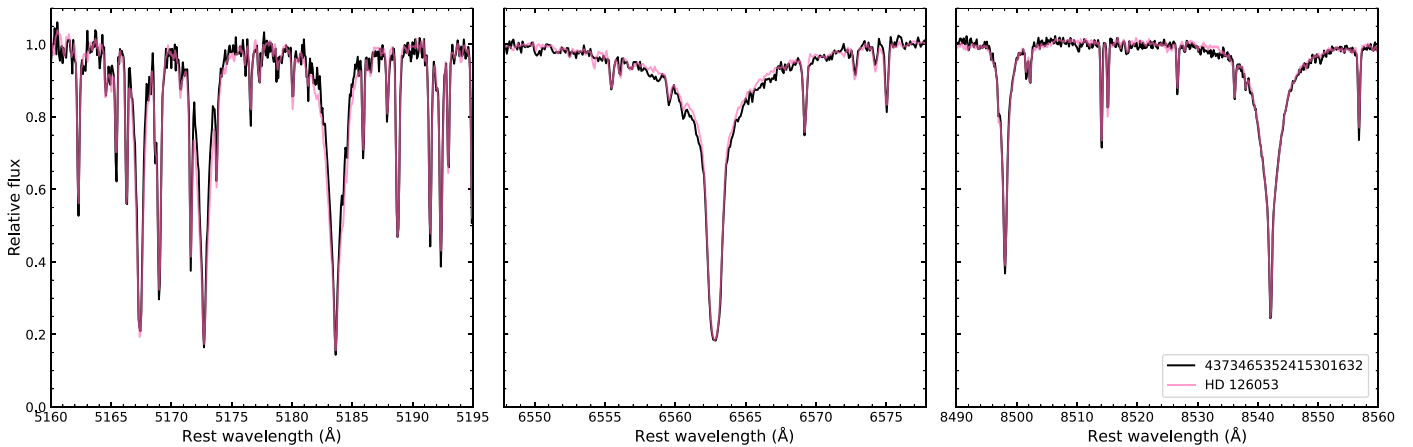


Figure 3. Selected portions of the Magellan/MIKE spectrum of Gaia DR3 4373465352415301632 (from left-hand to right-hand: the Mg triplet lines, $H\alpha$, and the Ca triplet). The spectrum of HD 126053, which has a spectral type of G1.5V (Gray et al. 2003), is overplotted in pink as a comparison. The close resemblance between the two stars in terms of line strengths and profiles is evident. The stellar parameters of HD 126053 are $T_{\text{eff}} = 5700$ K, $\log g = 4.5$, $[\text{Fe}/\text{H}] = -0.35$ (e.g., Brewer et al. 2016, Casali20). The small deviations in the wings of some strong lines are likely caused by a combination of continuum normalization uncertainties and the ~ 200 K difference in temperature between the two stars.

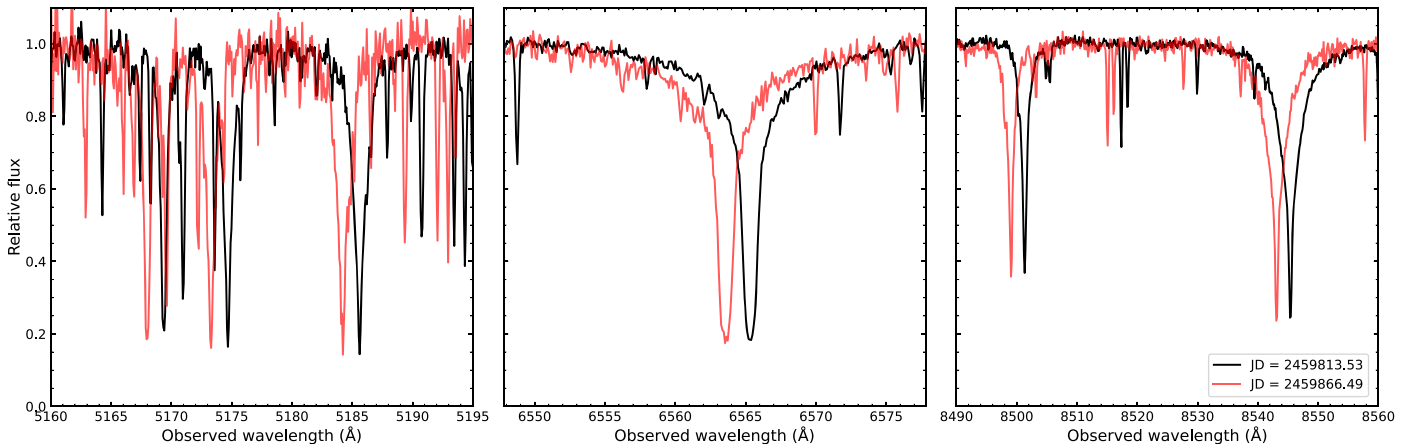


Figure 4. Selected portions of the Magellan/MIKE spectrum of Gaia DR3 4373465352415301632 (the Mg triplet lines, $H\alpha$, and the Ca triplet), shown here in the observed frame at the radial velocity extremes spanned by our data set.

parameters, search for signatures of a second luminous component in the binary, and measure the radial velocity as a function of time. We observed the star for five epochs with the Automated Planet Finder (APF) telescope (Vogt et al. 2014) at Lick Observatory, four epochs with the DEIMOS spectrograph (Faber et al. 2003) on the Keck II telescope, and obtained a high signal-to-noise ratio spectrum with the MIKE spectrograph (Bernstein et al. 2003) on the Magellan/Clay telescope (as well as a second, shorter MIKE spectrum) at Las Campanas Observatory.

The APF observations employed the Levy Spectrometer (Radovan et al. 2010) with a $2'' \times 8''$ slit, providing $R = 80,000$ spectra covering 3730–10200 Å. We observed Gaia DR3 4373465352415301632 on 2022 June 28, 2022 August 28, 2022 September 2, 2022 September 12, and 2022 October 4, obtaining three 1000 s exposures per epoch. The APF spectra were reduced with the California Planet Search pipeline (Butler et al. 1996; Howard et al. 2010; Fulton et al. 2015).

We observed Gaia DR3 4373465352415301632 with Magellan/MIKE for 2700 s on 2022 August 22, using a $0''.7$ slit to obtain an $R \approx 30,000$ spectrum from 3300 to 9400 Å. We reduced the MIKE spectrum with the Carnegie Python data reduction package (Kelson 2003). To provide a comparison

spectrum, we also obtained MIKE observations of the G1.5V radial velocity standard star HD 126053. Portions of the spectra of these two stars are displayed in Figure 3. We also observed Gaia DR3 4373465352415301632 for 745 s with MIKE during twilight on 2022 October 13 to obtain an additional velocity measurement. Figure 4 compares the two MIKE spectra of Gaia DR3 4373465352415301632, which represent the radial velocity extremes in our data set.

We observed Gaia DR3 4373465352415301632 with DEIMOS on 2022 September 19, 2022 September 24, 2022 September 27, and 2022 October 28 using the 1200G grating and a $0''.7$ long slit to obtain $R \approx 7000$ spectra from 6500–9000 Å. A single 300 s exposure was obtained in twilight on each night. We reduced the data with a modified version of the DEEP2 reduction pipeline (Cooper et al. 2012; Newman et al. 2013; Kirby et al. 2015). The long-slit mask employed for these observations did not contain enough slits to adequately constrain the quadratic correction to the sky line wavelengths as a function of position on the mask described by Kirby et al. (2015). Instead, we examined the night sky emission line wavelengths in the extracted spectrum, and used the measured wavelength shifts near the A-band and Ca triplet lines (which ranged from 0 to 4 km s^{-1}) to correct the wavelength scale.

2.2.2. Velocity Measurements

We measured the velocity of Gaia DR3 4373465352415301632 from the APF and MIKE spectra by performing χ^2 fits to high S/N spectra of radial velocity standard stars shifted to the rest frame. The velocity template for the MIKE spectra was HD 126053, for which we assumed a velocity of $v_{\text{hel}} = -19.21 \text{ km s}^{-1}$ from Gaia DR3, which is in excellent agreement with the measurement of $v_{\text{hel}} = -19.45 \text{ km s}^{-1}$ from Stefanik et al. (1999). For the APF velocity measurements, we used an APF observation of the G2V standard star HD 12846 (Gray et al. 2003; Soubiran et al. 2018). We assumed the Gaia DR3 velocity of $v_{\text{hel}} = -4.65 \text{ km s}^{-1}$, which is within 0.2 km s^{-1} of the pre-Gaia measurement of Soubiran et al. (2018). The fit procedures were based on those described by Simon et al. (2017) and subsequent papers, adapted for echelle spectroscopy. We fit each order of the target spectra independently with the matching order of the template spectrum, discarding orders, or portions of orders affected by telluric or interstellar absorption. For the MIKE observation, we only used the data from the red spectrograph (covering $\sim 4900\text{--}8900 \text{ \AA}$) for velocities because the stellar continuum was more difficult to define at blue wavelengths and the 23 clean red orders already provided plenty of signal. The S/N of the APF data was much lower but the velocity could still be determined accurately over ~ 30 spectral orders from ~ 4500 to 6800 \AA . For each observation, we averaged the velocities from all of the measured orders. The resulting statistical uncertainty was $\sim 0.1 \text{ km s}^{-1}$ for both the MIKE spectrum and the APF spectra. However, we imposed a systematic error floor of 1.0 km s^{-1} for MIKE based on the results of Ji et al. (2020). Given the potential for velocity offsets between different instruments, we assumed the same minimum uncertainty of 1.0 km s^{-1} for the APF observations.

For the DEIMOS spectrum, we used the set of radial velocity templates described by Kirby et al. (2015), fitting only to the Ca triplet wavelength range. We found that the metal-poor K1 dwarf HD 103095 produced the best match to the Gaia DR3 4373465352415301632 spectrum, so we used that template to determine the velocity. The velocity of the HD 103095 template spectrum was tied to that of the metal-poor giant HD 122563, for which we assumed a velocity of -26.51 km s^{-1} (Chubak et al. 2012), which agrees with the Gaia measurements within 0.4 km s^{-1} . We corrected for slit centering errors by carrying out a separate fit to the telluric A-band absorption of the rapidly rotating star HR 7346 (Simon & Geha 2007; Sohn et al. 2007). Based on the scatter of sky lines around their true wavelengths, we assume a velocity uncertainty of 2.0 km s^{-1} for each DEIMOS measurement (see Simon & Geha 2007; Kirby et al. 2015).

All of our velocity measurements, along with the two archival data points from LAMOST DR7 (Cui et al. 2012; Luo et al. 2022), are listed in Table 2.

3. Results and Analysis

3.1. The Spectral Energy Distribution

All of the archival photometry of Gaia DR3 4373465352415301632 that we were able to locate, including measurements from GALEX (Morrissey et al. 2007), SDSS DR16 Ahumada et al. 2020, APASS DR10 (Henden 2019), Pan-STARRS DR2 (Flewelling et al. 2020), SkyMapper DR2 (Onken et al. 2019), 2MASS (Cutri et al. 2003), and WISE

Table 2
Radial Velocity Measurements for Gaia DR3 4373465352415301632

Julian Date	Heliocentric Velocity (km s^{-1})	Velocity Uncertainty (km s^{-1})	Telescope/Instrument
2457881.29	20.0	4.1	LAMOST
2458574.36	8.9	5.6	LAMOST
2459758.93	50.5	1.0	APF
2459813.53	90.3	1.0	Magellan/MIKE
2459819.68	67.6	1.0	APF
2459825.76	49.4	1.0	APF
2459835.65	31.0	1.0	APF
2459842.72	22.6	2.0	Keck/DEIMOS
2459847.71	17.6	2.0	Keck/DEIMOS
2459850.71	15.4	2.0	Keck/DEIMOS
2459857.65	13.1	1.0	APF

(Cutri et al. 2021) is displayed in Figure 2 and listed in Table 1. As is clear, the SkyMapper v , i , z bands are discrepant with other photometric measurements at comparable wavelengths, and we therefore exclude them from our SED fits. Using the publicly available SED fitting code ARIADNE (Vines & Jenkins 2022), we fit the observed photometry (excluding SkyMapper and the wide Gaia bands) to derive stellar parameters. Although Gaia offers extremely precise optical photometry of Gaia DR3 4373465352415301632, we note that there may be contamination in the G_{BP} and G_{RP} bands as a result of the star's location in the direction of the Galactic bulge. The $\text{phot_bp_rp_excess_factor}$ for this source is 1.24 and the $G_{\text{BP}} - G_{\text{RP}}$ color is 1.17, which indicates that the blending probability is $\sim 30\%$ (Riello et al. 2021).

The resultant posterior distributions are shown in the corner plot for the stellar parameters, along with the best-fit extinction in Figure 5. ARIADNE fits broadband photometry to a variety of stellar atmosphere models. In this case, the best fit is obtained with the Phoenix models (Husser et al. 2013). Here, we have used a prior on the distance that is consistent with the measured Gaia parallax for this source. Including the Gaia G -band magnitude in the fit does not significantly change any of the derived parameters. We obtain similar values for the effective temperature and other derived parameters when only fitting to GALEX photometry, along with B and V bands from APASS, SDSS g , r , i , z , 2MASS J , H , K_s , and WISE photometry. Similar posterior distributions are also obtained if Pan-STARRS photometry is used instead of SDSS. The best-fit ARIADNE parameters are: $T_{\text{eff}} = 5796_{-153}^{+93} \text{ K}$, $\log g = 4.26_{-0.27}^{+0.24}$, $R = 1.02_{-0.029}^{+0.031} R_{\odot}$, and $[\text{Fe}/\text{H}] = -0.24_{-0.08}^{+0.09}$. As the corner plot shows, the posterior distributions are tightly constrained. The SED fit, along with the residuals, is shown in the bottom panel of Figure 5.

We have also used the BaSeL model spectral library (Lejeune et al. 1997, 1998) to fit the observed photometry with both a combined χ^2 and genetic algorithm optimization and a Markov Chain Monte Carlo (MCMC) approach. Here we assume a Fitzpatrick (1999) extinction law with $R_V = 3.1$ and reddening $E(B - V) = 0.3 \text{ mag}$. The best-fit SEDs are shown in Figure 6(a) for a single source. The fit assuming two sources is shown in Figure 6(b). In the single-source case, we obtain a reduced χ^2 of 3.7, best-fit parameters $T_{\text{eff}} = 5927 \text{ K}$, $\log g = 4.0$, $L = 1.08 L_{\odot}$, and metallicity of $Z = 0.009$. For a two source fit, we obtain a reduced χ^2 of 5.5, with $T_{\text{eff}} = 6241 \text{ K}$, $\log g = 4.99$,

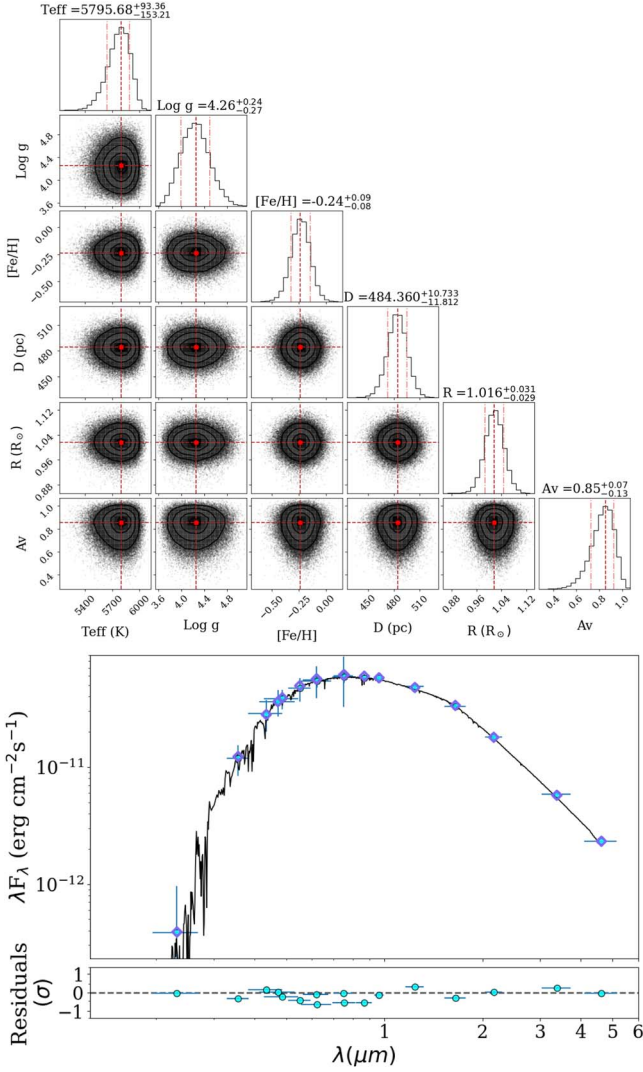


Figure 5. (Top) Posterior distributions of stellar parameters from ARIADNE using all of the available photometry except SkyMapper and Gaia, with the distance prior set from the measured Gaia parallax. (Bottom) Resultant best-fit SED. There is no evidence for an excess at short or long wavelengths that could indicate a second source contributing to the observed fluxes. The same points are shown in the residual plot below in circles (in the SED plot, they are overlotted with diamonds).

$L = 0.42 L_{\odot}$, and $Z = 0.0006$ for the hotter component and $T_{\text{eff}} = 5763$ K, $\log g = 4.01$, $L = 0.67 L_{\odot}$, and $Z = 0.01$ for the cooler component. Although the raw χ^2 value does improve upon adding a second component (17 for the composite spectrum versus 25 for the single SED fit), this is not enough to compensate for the increase in the number of model parameters in the reduced χ^2 . Therefore, we conclude that there is no significant evidence in the SED for the presence of more than one luminous component.

3.2. Spectroscopic Analysis and Stellar Parameter Estimation

3.2.1. Full Spectral Fitting

Visual examination of the MIKE spectrum of Gaia DR3 4373465352415301632 shows that it closely resembles an early G star (see Figure 3). No sign of a secondary component is visible in either the metallic or hydrogen lines. Given the spectral resolution, a companion star that makes a

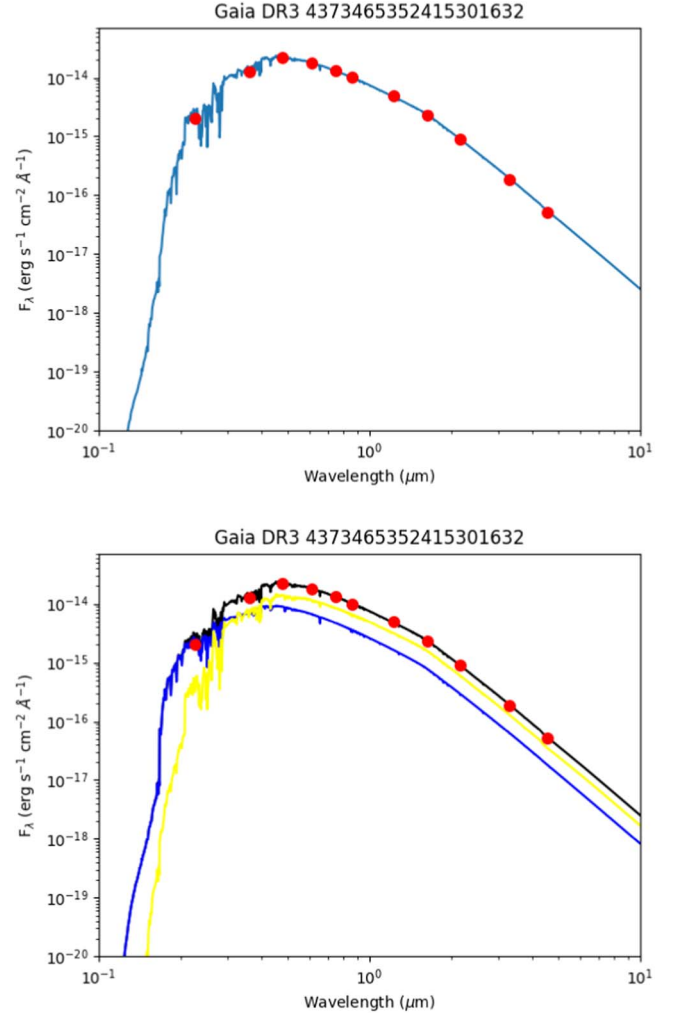


Figure 6. (a) Single SED fit using the BaSeL model and the Fitzpatrick (1999) extinction law. (b) Composite SED fit, with the cooler component shown in yellow, the hotter component shown in blue, and the composite spectrum shown in black.

nonnegligible contribution to the flux should be detectable unless its velocity is within ~ 10 km s⁻¹ of that of the primary. As we will show later on, the velocity of the primary at the time of observation was more than 40 km s⁻¹ away from the center-of-mass velocity of the system (also see Figure 4), which indicates that the secondary spectrum should be resolvable from the primary at this epoch if it is a luminous main-sequence star.

To provide an initial estimate of the stellar parameters from its spectrum rather than the broadband photometry, we fit the MIKE spectrum with the empirical spectral fitting code SpecMatch-Emp (Yee et al. 2017). Using the spectral range 5100–5700 Å, the best-fit parameters determined from a linear combination of stars in the template library are: $T_{\text{eff}} = 5917 \pm 110$ K, $R = 1.20 \pm 0.18 R_{\odot}$, $\log g = 4.24 \pm 0.14$,¹⁶ and $[\text{Fe}/\text{H}] = -0.22 \pm 0.09$, with HD 44985 as the single closest match to Gaia DR3 4373465352415301632. These parameters are in excellent agreement with those from the SED fit.

¹⁶ To determine $\log g$, we make use of the result from the detailed spectroscopic analysis (which follows) that the mass of the star is $0.91 M_{\odot}$.

Table 3
Derived Stellar Parameters

Property	Value	Unit
Effective temperature (T_{eff})	5972 ± 100	K
Surface gravity ($\log g$)	4.54 ± 0.15	$\log \text{cm s}^{-2}$
Metallicity ([Fe/H])	-0.30 ± 0.10	
Microturbulent velocity (ξ)	1.10 ± 0.10	km s^{-1}
Stellar mass (M_*)	0.91 ± 0.10	M_{\odot}
Stellar radius (R_*)	1.003 ± 0.075	R_{\odot}
Luminosity (L_*)	1.186 ± 0.232	L_{\odot}
Isochrone-based age (τ_{iso})	7.1 ± 3.8	Gyr

Note. The parameters that are listed here are determined via the combined analysis of the high-resolution stellar spectrum along with theoretical isochrones, as described in Section 3.2.2.

3.2.2. Fundamental and Photospheric Stellar Parameters

Next, we determined the stellar parameters of Gaia DR3 4373465352415301632 more rigorously using a combination of the classical spectroscopic approach¹⁷ and a comparison with theoretical isochrones to infer accurate, precise, and self-consistent parameters.

The inputs to this parameter inference procedure include the equivalent widths of Fe I and Fe II atomic absorption lines, as well as multiwavelength photometry from Gaia DR3 *G*-band (Riello et al. 2021) and 2MASS (*J*, *H*, and *Ks*), the Gaia DR3 parallax (Lindgren et al. 2021b), and we adopt the *V*-band extinction from the three-dimensional Stilism reddening map (Lallement et al. 2014; Capitanio et al. 2017; Lallement et al. 2018). The absorption line data are based on the line lists presented in Meléndez et al. (2014) and Reggiani & Meléndez (2018). We measured the equivalent widths by fitting Gaussian profiles with the Spectroscopy Made Harder (*smhr*) software package to the continuum-normalized MIKE spectrum. The continuum normalization was performed using *smhr*. We assume solar abundances from Asplund et al. (2021) and follow the steps described in Reggiani et al. (2022b, 2022a) to obtain the fundamental and photospheric stellar parameters from a combination of spectral information and a fit to the MESA Isochrones and Stellar Tracks (Choi et al. 2016) stellar models. We do the fitting with the *isochrones* package¹⁸ (Morton 2015), which uses *Multinest*¹⁹ (Feroz & Hobson 2008; Feroz et al. 2009, 2019) via *PyMultinest* (Buchner et al. 2014).

Our derived fundamental and photospheric parameters for Gaia DR3 4373465352415301632 are listed in Table 3. Its position relative to the MIST isochrones is illustrated in Figure 7. The effective temperature is in excellent agreement with the values determined from the single-source SED fit, as well as the full spectral fitting. According to the effective temperature calibration given by Gray & Corbally (2009), the spectral classification would be G0. The surface gravity that is required to enforce ionization balance on the Fe lines is somewhat higher than determined via other techniques, but the disagreement is only at the 1.6σ level. The spectroscopic metallicity of Gaia DR3 4373465352415301632 is also modestly lower than the photometric value. The overall good

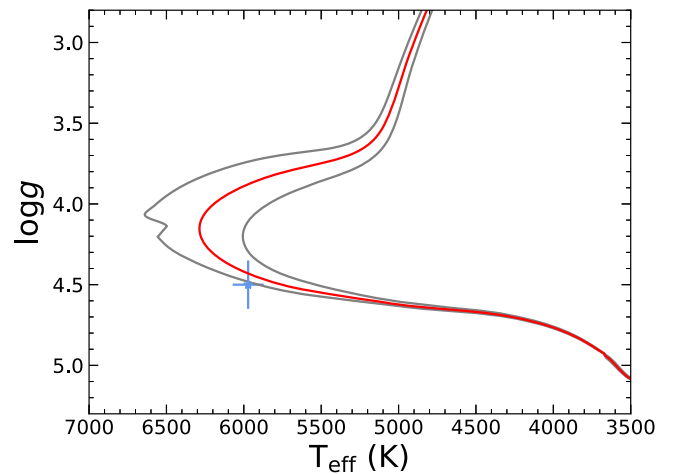


Figure 7. Effective temperature and surface gravity of Gaia DR3 4373465352415301632 compared to MIST isochrones. The blue point shows the derived position of the star and the red curve is the $0.91 M_{\odot}$ isochrone that provides the best fit to the combined photometric and spectroscopic data. The gray curves represent $0.89 M_{\odot}$ and $0.93 M_{\odot}$ isochrones for comparison.

agreement on the stellar parameters that is achieved through multiple independent methods indicates that systematic uncertainties, e.g., related to the choice of stellar evolution tracks, are smaller than the adopted uncertainties (Table 3). We conclude that Gaia DR3 4373465352415301632 is an old, moderately metal-poor main-sequence star, which is slightly less massive than the Sun.

3.2.3. Chemical Abundances

We used the photospheric stellar parameters from Table 3 to calculate the abundances of C I, O I, Na I, Mg I, Al I, Si I, S I, K I, Ca I, Sc II, Ti I, Ti II, V I, Cr I, Cr II, Mn I, Fe I, Fe II, Co I, Ni I, Cu I, Zn I, Sr II, Y II, Zr II, Ba II, and Ce II, from the equivalent widths (EWs) of spectroscopic absorption lines. We measured equivalent widths from the continuum-normalized MIKE spectrum by fitting Gaussian profiles with *smhr*. We use the one-dimensional plane-parallel, α -enhanced, ATLAS9 model atmospheres (Castelli & Kurucz 2003) and the 2019 version of MOOG (Snedden 1973) to infer elemental abundances based on each equivalent width measurement, while initially assuming local thermodynamic equilibrium (LTE). Our calculations include hyperfine structure splitting for Sc II (based on the Kurucz line list²⁰), V I (Prochaska et al. 2000), Mn I (Prochaska & McWilliam 2000; Blackwell-Whitehead et al. 2005), Cu I (Prochaska et al. 2000, and Kurucz line lists), and Y II (Kurucz line lists), and we account for isotopic splitting for Ba II (McWilliam 1998). We report the adopted atomic data, equivalent width measurements, and individual line-based abundances in Table 4. Our final abundances are reported in Table 5.

When possible, we update our elemental abundances derived under the assumptions of LTE to account for departures from LTE (i.e., non-LTE corrections) by interpolating published grids of non-LTE corrections for several elements. We make use of three-dimensional non-LTE corrections for carbon and oxygen (Amarsi et al. 2019), and one-dimensional non-LTE corrections for sodium (Lind et al. 2011), aluminum (Amarsi et al. 2020), silicon (Amarsi & Asplund 2017), potassium (Reggiani et al. 2019), calcium (Amarsi et al. 2020), iron

¹⁷ Based on simultaneously minimizing the difference between the abundances determined from Fe I and Fe II lines, as well as their dependencies on transition excitation potential and reduced equivalent width.

¹⁸ <https://github.com/timothydmorton/isochrones>

¹⁹ <https://ccpforge.cse.rl.ac.uk/gf/project/multinest/>

²⁰ <http://kurucz.harvard.edu/linelists.html>

Table 4
Atomic Data, Equivalent Widths and Line Abundances

Wavelength (Å)	Species	Excitation Potential (eV)	log(<i>g</i> f)	EW (mÅ)	log(ϵ_X)
6154.225	Na I	2.102	-1.547	20.80	5.993
6160.747	Na I	2.104	-1.246	31.52	5.927
4571.095	Mg I	0.000	-5.623	89.51	7.395
4730.040	Mg I	4.340	-2.389	43.79	7.381
5711.088	Mg I	4.345	-1.729	80.01	7.244
6318.717	Mg I	5.108	-1.945	26.75	7.284
5260.387	Ca I	2.521	-1.719	23.01	6.139
5512.980	Ca I	2.933	-0.464	63.20	5.966

Note. Full version online. This table will be published in its entirety as a machine-readable table. A portion is shown here for guidance regarding its form and content.

(This table is available in its entirety in machine-readable form.)

(Amarsi et al. 2016), and barium (Amarsi et al. 2020). The NLTE-corrected abundances are listed in Table 5.

The abundance analysis shows that Gaia DR3 4373465352415301632 is a mildly α -enhanced star ($[\alpha/\text{Fe}] \sim 0.1$), as expected for its metallicity. The iron-peak and neutron-capture elemental abundances are also fully compatible with the typical values for this metallicity range, based on galactic chemical evolution models (e.g., Kobayashi et al. 2020) and large spectroscopic surveys (e.g., Amarsi et al. 2020). We do not see any sign of the large enhancements in light elements and α elements that have been detected in some X-ray binary companions (e.g., Orosz et al. 2001; González Hernández et al. 2008; Suárez-Andrés et al. 2015; Casares et al. 2017).

4. Orbit Fitting

Based on the Gaia astrometry and our radial velocity measurements, the binary orbit of Gaia DR3 4373465352415301632 can be determined astrometrically, spectroscopically, or using a combination of both types of data. To test the consistency of the velocities with the Gaia astrometric orbit, we consider each of these cases in turn. We fit Keplerian orbits to the RV data using the adaptation of the *orvara* code (Brandt et al. 2021) presented in Lipartito et al. (2021).

In this section, we briefly discuss the Gaia orbital constraints and then present our orbital fits using only RVs. For joint astrometric+spectroscopic fits, we cannot use *orvara* directly with Gaia astrometry because the individual astrometric measurements are not given in DR3. We have only a set of best-fit parameters and a covariance matrix. As a result, we incorporate constraints from Gaia by conditioning our RV fits on the Gaia results. (An alternate approximate approach would be to determine the times that targets cross the Gaia focal plane and then use that as an estimate of the times of observation.) We discuss this approach and our results in Section 4.3.

4.1. Astrometry Only

The Gaia DR3 *non_single_stars* catalog provides orbital parameters for Gaia DR3 4373465352415301632 based on a fit to the individual astrometric measurements obtained by Gaia. However, the astrometric measurements themselves will not be available until the fourth Gaia data release ~ 3 yr from the time

Table 5
Chemical Abundances

Species	<i>N</i>	log(ϵ_X)	[X/Fe]	$\sigma_{[X/Fe]}$
C I	4	8.01	-0.15	0.09
O I	3	8.65	0.26	0.03
Na I	2	5.96	0.04	0.03
Mg I	4	7.33	0.08	0.04
Al I	5	6.08	-0.05	0.02
Si I	11	7.27	0.06	0.03
S I	4	6.85	0.03	0.01
K I	1	5.18	0.42	0.01
Ca I	10	6.06	0.06	0.02
Sc II	4	2.94	0.10	0.09
Ti I	9	4.60	-0.07	0.03
Ti II	10	4.80	0.13	0.04
V I	3	3.51	-0.09	0.02
Cr I	8	5.26	-0.06	0.02
Cr II	5	5.24	-0.07	0.03
Mn I	6	4.88	-0.23	0.05
Fe I	79	7.16
Fe II	18	7.15
Ni I	14	5.94	0.04	0.03
Cu I	2	3.79	-0.09	0.02
Zn I	2	4.25	-0.01	0.07
Sr I	1	2.41	-0.12	0.00
Y II	3	1.82	-0.08	0.05
Zr II	1	2.29	-0.00	0.03
Ba II	3	2.12	0.15	0.05
Ce II	1	1.55	0.27	0.03
non-LTE Corrected Abundances				
C I	4	8.07	-0.04	0.16
O I	3	8.57	0.24	0.03
Na I	2	5.85	-0.01	0.04
Al I	2	6.07	0.00	0.01
Si I	11	7.25	0.10	0.08
K I	1	4.74	0.03	...
Fe I	79	7.18
Fe II	18	7.22
Ba II	3	1.96	0.06	0.03

of this writing. The parameters listed directly in the catalog include the period P , the time of periastron T_0 , the eccentricity e , the secondary mass M_2 , and the Thiele-Innes (TI) elements A , B , F , and G . Following the method of Binnendijk (1960), as presented by Halbwachs et al. (2022), we use the TI elements to compute the semimajor axis a , the position angle of the ascending node Ω , the longitude of periastron ω , and the inclination i . The values of these parameters are listed in Table 6. We note that these calculations are based on the results reported in the two body orbit catalog and the binary mass catalog from Gaia Collaboration et al. (2022a).

The TI elements, together with the eccentricity, describe an orbit in the plane of the sky. We generate 50 random realizations of measurements drawn from the Gaia best-fit values and covariance matrix. We then plot the sky paths given by the eccentricities and TI elements. Figure 8 shows these sky paths about the barycenter; the best-fit orbit reported by Gaia DR3 is shown as a thicker black line. The orbit has a semimajor axis of 2.98 ± 0.22 mas, with the major axis oriented nearly east-west.²¹

²¹ We note that the perpendicular orientation shown by El-Badry et al. (2023b) is a result of an inconsistency in a plotting routine (K. El-Badry 2023, private communication).

Table 6

Orbital Solutions for Gaia DR3 4373465352415301632 for the Data Set Listed in Table 2

Parameter	Value
Astrometric fit	
P	185.77 ± 0.31 day
T_0	2457377.0 ± 6.3 day
e	0.49 ± 0.07
a	2.98 ± 0.22 mas
i	121.3 ± 3.5
Ω	89.6 ± 3.8
ω	-10.6 ± 11.9
M_2	$12.8_{-2.3}^{+2.8} M_\odot$
RV fit	
P	$184.28_{-0.89}^{+0.75}$ day
T_0	2459802.4 ± 3.0 day
e	$0.41_{-0.021}^{+0.034}$
ω	$19^\circ_{-6.6}^{+6.0}$
K_1	$60.6_{-5.8}^{+10.0} \text{ km s}^{-1}$
γ	$47.8_{-1.4}^{+2.2} \text{ km s}^{-1}$
f	$3.2_{-0.9}^{+1.6} M_\odot$
Joint fit	
P	$185.41_{-0.087}^{+0.101}$ day
T_0	$2459757.9_{-1.5}^{+1.2}$ day
e	$0.456 \pm .023$
a	$1.357_{-0.061}^{+0.069}$ au
i	123.6 ± 1.6
Ω	$96^\circ_{-2.0}^{+2.3}$
ω	$10^\circ_{-2.0}^{+2.7}$
M_2	$11.33_{-1.32}^{+1.57} M_\odot$

4.2. Radial Velocity Data Only

We fit the radial velocity data using the adaptation of `orvara` (Brandt et al. 2021) described in Lipartito et al. (2021). This remains an MCMC-based fitting approach but differs from the main version of `orvara` in several ways:

1. It fits only for the RV parameters of period, eccentricity, RV semi-amplitude, periastron time, argument of periastron, and RV zero-point;
2. The argument of periastron refers to the star (as is the definition for Gaia astrometry); and
3. Only the RV zero-point (barycenter RV of the system) is analytically marginalized off.

We use uniform priors on all of the RV parameters: period, semi-amplitude, eccentricity, periastron time, RV zero-point, and (stellar) argument of periastron. We find a highly multimodal posterior, with orbital solutions at periods of ~ 142 days, ~ 164 days, ~ 184 days, ~ 220 days, and additional possible periods out to at least 1000 days. The top panel of Figure 9 shows the wide range of RV orbits consistent with our Gaia DR3 4373465352415301632 velocities. The fits to the data are satisfactory, with a best-fit χ^2 of 3 for 13 data points with six free parameters, i.e., seven degrees of freedom.

Because one of our main goals is to determine whether the Gaia astrometric orbital solution is correct, we restrict the subsequent analysis of our RV data to solutions with a period range within ± 10 days of the Gaia orbital period of ~ 185 days, discarding those with shorter or longer periods. A similar procedure was adopted by El-Badry et al. (2023b) in their analysis because their RV data (although more extensive than

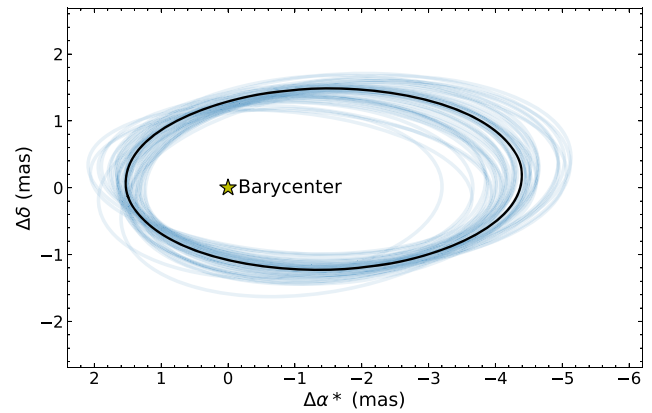


Figure 8. Astrometric orbit determined from the Gaia DR3 astrometric orbital solution as described in the text. The best-fit orbit calculated directly from the Gaia parameters is plotted as the thick black curve, and the thin blue curves represent orbits drawn randomly from the posterior distribution.

ours) also yields multiple period solutions. However, as we note below, the combination of our RV data and that of El-Badry et al. (2023b) gives a unimodal solution for the period, which is not possible using either data set alone. This result is illustrated in Figure 9b, where the combined RV data uniquely determine the orbital period without reference to the Gaia astrometric solution. The fit to the combined RV data set remains formally good, with a best-fit χ^2 of 24 for 52 total radial velocity measurements and six free parameters (46 degrees of freedom). The low χ^2 value suggests that, if anything, the RV errors and, by extension, our derived parameter uncertainties, may be overestimated.

The spectroscopic orbital parameters from the MCMC fit to our RV data set (the velocities listed in Table 2), restricted to periods between 175 and 195 days, are listed in the second section of Table 6. Figure 10 shows the corner plot of the posterior distribution. Using all of the available RVs gives the posterior distributions shown in Figure 11 and the best-fit parameters listed in the top section of Table 7, whereby the combination of both data sets yields very precise constraints on all parameters that can be determined with RV data. The radial velocity curve and the phase-folded radial velocity curve with residuals are displayed in Figure 12 for both our RV data alone and all available RV data. Although our RV data allow a wide range of possible orbits, especially at phases near 0 and 1, the inclusion of data from El-Badry et al. (2023b) restricts the range of possible orbits significantly. Just 0.4% of the points in the chain lie away from the mode at $P \approx 185$ days, and are in a much sparser cluster at $P \approx 218$ days. We obtain very similar results using different orbit-fitting packages such as `TheJoker` (Price-Whelan et al. 2017) or `exoplanet` (Foreman-Mackey et al. 2021a, 2021b).

The mass function derived from our period-restricted spectroscopic orbital solution is $f = 3.2_{-0.9}^{+1.6} M_\odot$. When combined with the primary mass determined from the spectral analysis, the corresponding minimum secondary mass is $4.6 M_\odot$, which is consistent with the companion being a black hole. However, because our spectroscopic measurements missed the maximum radial velocity at the periastron of the orbit, our constraint on the velocity semi-amplitude K_1 is not very strong, as is apparent from the definition of the mass

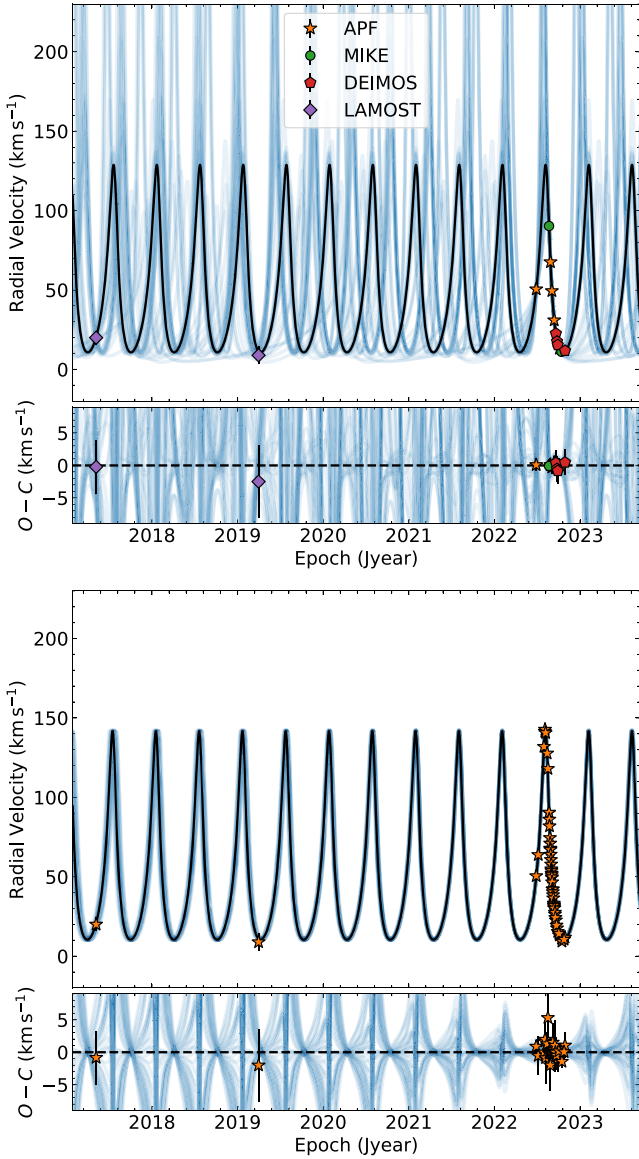


Figure 9. (Top) Radial velocity solution for Gaia DR3 4373465352415301632, for the velocity measurements listed in Table 2. The black curve is the most likely MCMC orbital solution determined from the spectroscopic measurements alone, and the light-blue curves are a random set of MCMC samples. Many periods are consistent with the RV data. (Bottom) Radial velocity solution including data from Table 2 and from El-Badry et al. (2023b). This fit yields a unimodal solution for the period even without incorporating any information from the astrometric solution (0.4% of the points in the chain are at $P \approx 218$ day).

function:

$$f = \frac{PK_1^3}{2\pi G} (1 - e^2)^{3/2} = \frac{M_2^3 \sin^3 i}{(M_1 + M_2)^2}, \quad (1)$$

where P is the orbital period, and M_1 and M_2 are the masses of the two stars. The cubic dependence of the mass function on K_1 then results in a large uncertainty in the mass function and the mass of the secondary, such that with our radial velocities alone we cannot completely exclude masses below $4 M_\odot$. The derived constraints on the spectroscopic mass function improve significantly when using all available RV data, while combining our measurements and those from El-Badry et al. (2023b). In this case, we obtain $f = 3.9 \pm 0.04 M_\odot$, which implies a

secondary mass of $9.2 M_\odot$ (when the astrometric inclination is included).

4.3. Joint Fits

Our joint fits rely on determining the set of orbits that simultaneously satisfy constraints from both the RV data and the Gaia astrometry. We begin with the MCMC chains derived from RVs alone and then condition these chains on the Gaia astrometry. We achieve this by first choosing random values for parameters unconstrained by RV: parallax, inclination, and position angle of the ascending node. With a random set of these parameters for each step of the chain, we can compute the TI constants and use the Gaia DR3 covariance matrix to compute a likelihood. We then re-weight each step of the chain by its corresponding likelihood. In practice, we improve our signal-to-noise ratio by choosing many possible inclinations, position angles, and parallaxes for each step of the RV chain, and computing the Gaia likelihood for each of them.

Our conditioning of the RV fits on the Gaia covariance matrix immediately reveals a problem. If we adopt the full RV data set—the union of our data and that of El-Badry et al. (2023b)—, then the goodness-of-fit is formally good for the RVs ($\chi^2 = 24$ for 46 degrees of freedom). The step in this chain that agrees best with Gaia, even when freely choosing inclination, position angle, and parallax, has a χ^2 with respect to Gaia of 11 with five degrees of freedom. This step is, in turn, a much worse fit to the RVs, with $\Delta\chi_{\text{RV}}^2 \approx 12$. The Gaia constraint provides an additional five degrees of freedom but increases the total χ^2 by about 20. This would be even worse if the RV errors are underestimated, as suggested by the low χ^2 for the RV-only fit.

The poor formal agreement of Gaia astrometry with the RVs renders any resulting confidence intervals dubious. The increases in χ^2 from conditioning on Gaia are about a factor of 4 larger what is expected; this suggests that the Gaia uncertainties are underestimated by a factor of ≈ 2 . Figure 13 shows this tension in the five parameters constrained both by astrometry and radial velocities; the RV confidence intervals are from the entire RV data set. The 1σ confidence intervals do not overlap in any parameters apart from eccentricity. (We emphasize, though, that both the astrometry and RV data sets independently point to Gaia DR3 4373465352415301632 containing a $\sim 10 M_\odot$ black hole with a ~ 185 day period. The disagreement that is discussed here only relates to determining the exact orbital parameters of the system.)

Based on the combined evidence from a satisfactory fit to the RV data and an unsatisfactory joint fit, we inflate the Gaia uncertainties by a factor of 2. We retain the form of the Gaia covariance matrix (i.e., the correlation coefficients between parameters) and simply multiply this matrix by a factor of 4. This increase in the uncertainties leads to acceptable joint fits, with χ^2 increasing by ≈ 8 when optimizing the best-fit orbit with the additional five degrees of freedom provided by astrometry.

We therefore adopt the following prescription to condition the RV fits on the Gaia astrometry:

1. We select many possible sets of random values for parallax, position angle, and inclination for each step in an RV chain;

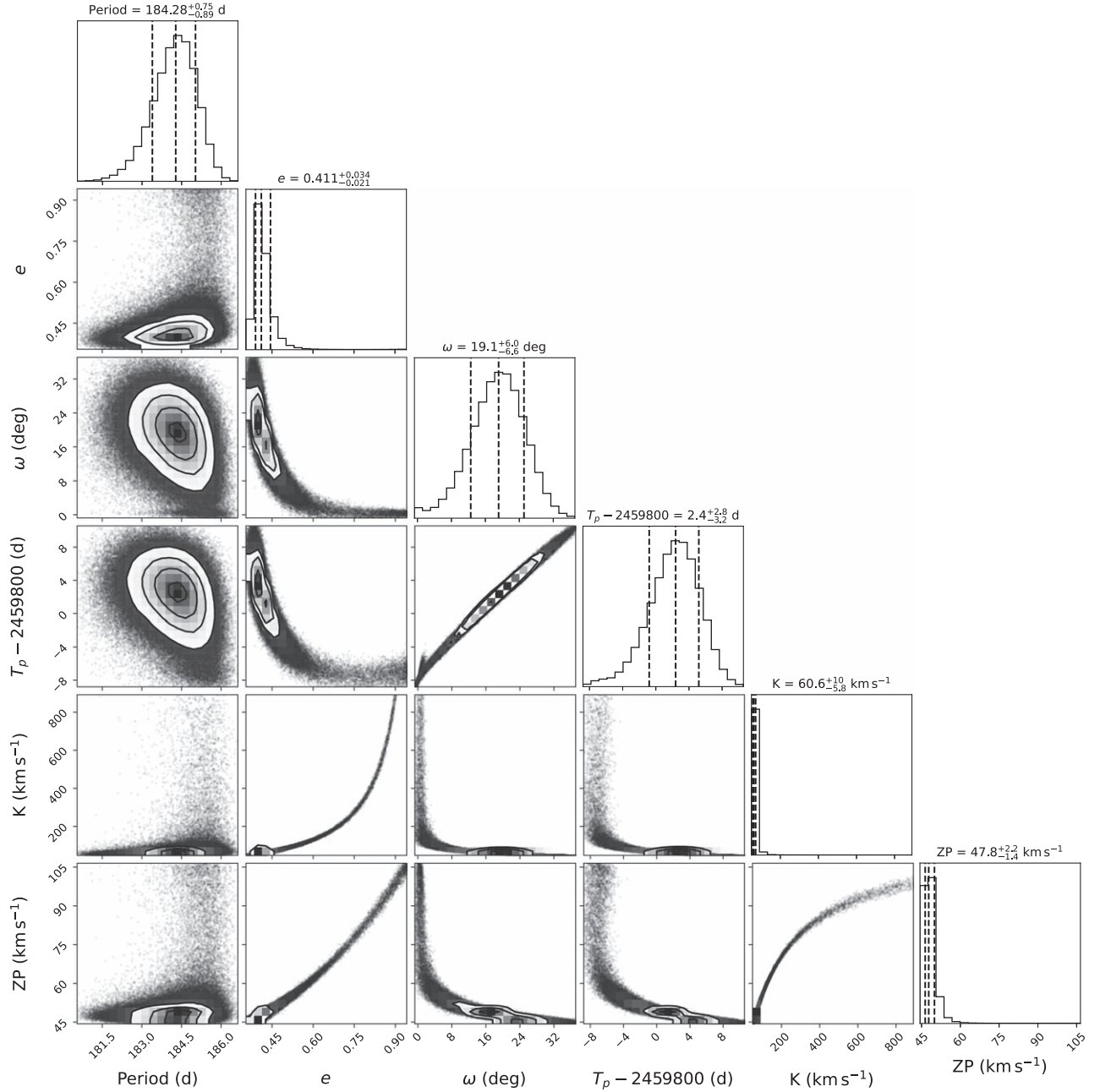


Figure 10. MCMC results for the orbital solution determined from the radial velocity data listed in Table 2, showing only elements in the chain with periods between 175 and 195 days. Although some of the parameters exhibit significant correlations, the overall orbital properties are well constrained by the data, with results similar to those expected from the astrometric solution. Some parameters, such as K_1 , do have significant uncertainties.

2. We compute the TI constants and evaluate

$$\chi^2 = (\mathbf{p} - \tilde{\mathbf{p}})^T \mathbf{C}_{\text{Gaia}}^{-1} (\mathbf{p} - \tilde{\mathbf{p}}), \quad (2)$$

where \mathbf{p} is the set of parameters from the RV chain (including the additional parameters above), $\tilde{\mathbf{p}}$ are the best-fit Gaia values, and \mathbf{C}_{Gaia} is the Gaia covariance matrix; and

3. We weight each of these steps by $e^{(-\chi^2/8)}$, equivalent to multiplying the Gaia covariance matrix by 4 (or doubling the uncertainties). This produces a weighted chain.

Figure 14 presents another way of visualizing the resulting combined constraints and the tension of Gaia with the RVs. The top panel shows a random sampling of the astrometric

orbits that are compatible with both the union of the RV data sets and the Gaia covariance matrix. It is more tightly constrained than the orbits shown in Figure 8 but less so than those shown in El-Badry et al. (2023b) due to our inflation of the Gaia uncertainties. We note that El-Badry et al. (2023b) did perform a check with inflated uncertainties but used the published Gaia covariance matrix for their baseline case. The lower two panels of Figure 14 show the tension between the astrometry and RVs. The black lines, denoting the steps in the RV chains that best match the Gaia astrometry, leave systematics in the RV residuals. This is true both when using only our RVs (middle panel) and using all RVs (lower panel). The light-blue lines are randomly drawn from the weighted

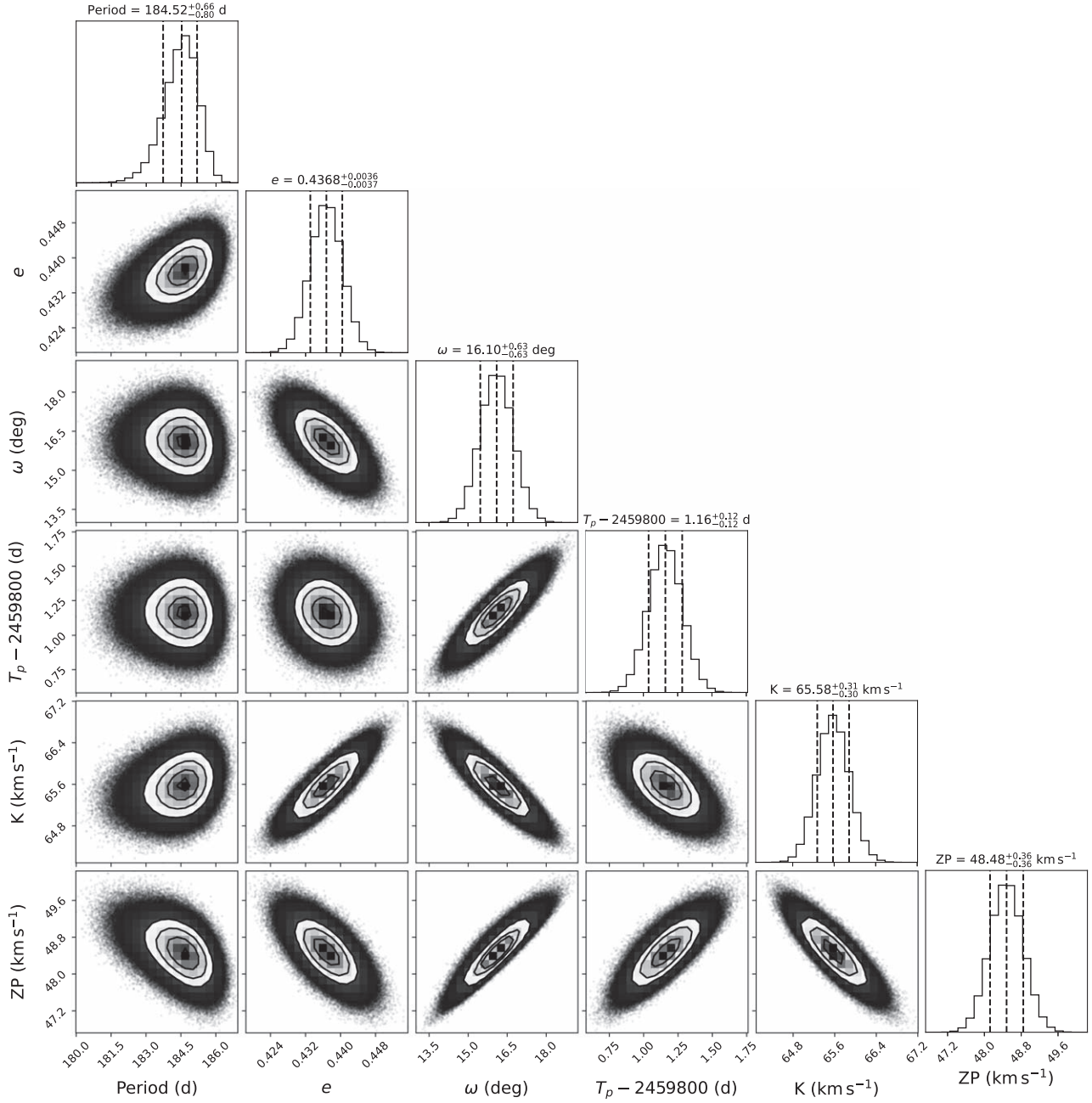


Figure 11. MCMC results for the orbital solution determined from all available radial velocity data, including the measurements from El-Badry et al. (2023b). The orbital solution is much more strongly constrained by the full data set. We do not show a much sparser cluster of points at $P \approx 218$ days, which contains $\approx 0.4\%$ of the chain.

chains computed as described earlier. These RV residuals can be compared to those shown in Figure 12 for the best fit to the RVs alone.

Our joint constraints for Gaia DR3 4373465352415301632 using both our radial velocity data and the astrometry are listed in Table 6 (which also provides the astrometric fit and posteriors that result from fitting to the velocities only). Figure 15 displays the resultant corner plot for the derived parameters of the combined fit using the RV data listed in Table 2. We find that the secondary mass of Gaia DR3 4373465352415301632 is $11.64^{+1.52}_{-1.31} M_{\odot}$. Using all of the available radial velocity data gives the posterior distributions shown in Figure 16 and the parameters listed in the bottom section of Table 7, leading to a smaller secondary mass of

$9.326^{+0.216}_{-0.209} M_{\odot}$, which is in closer agreement with El-Badry et al. (2023b).

5. Discussion

As noted in Section 1, during the preparation of this manuscript, on 2022 September 14 El-Badry et al. (2023b) submitted to MNRAS and posted a preprint of an analysis of this same source selected from the Gaia DR3 catalog. The overall conclusions of the two studies are in good agreement—the spectroscopic and astrometric measurements of Gaia DR3 4373465352415301632 both independently and together demonstrate that the companion is a massive black hole. El-Badry et al. (2023b) have a much more accurate RV-only

Table 7
Orbital Solutions for Gaia DR3 4373465352415301632 Using All Available Data

Parameter	Value
RV fit	
P	$184.52^{+0.66}_{-0.80}$ day
T_0	2459801.16 ± 0.12 day
e	$0.4368^{+0.0036}_{-0.0037}$
ω	$16^\circ 10 \pm 0.63$
K_1	$65.58^{+0.31}_{-0.30}$ km s $^{-1}$
γ	$48.48^{+0.36}_{-0.36}$ km s $^{-1}$
f	$3.92^{+0.042}_{-0.042} M_\odot$
Joint fit	
P	$185.52^{+0.08}_{-0.08}$ day
T_0	2459759.3 ± 1.1 day
e	$0.439^{+0.003}_{-0.003}$
a	$1.258^{+0.011}_{-0.010}$ au
i	$126^\circ 80^{+0.62}_{-0.63}$
Ω	$98^\circ 71^{+1.97}_{-2.01}$
ω	$15^\circ 89 \pm 0.61$
M_2	$9.326^{+0.216}_{-0.208} M_\odot$

solution thanks to their extensive RV coverage. Based on our joint fits to our RV data and astrometry, we infer a companion mass of $11.64^{+1.52}_{-1.31} M_\odot$, whereas El-Badry et al. (2023b) report a lower companion mass of $9.62 \pm 0.18 M_\odot$. As noted earlier, our observations did not cover the peak of the radial velocity curve, which limited the precision with which we can determine the velocity semi-amplitude of the primary. Consequently, the best-fit peak-to-trough amplitude of the orbital solution using our RV data is ~ 160 km s $^{-1}$, compared to ~ 140 km s $^{-1}$ in El-Badry et al. (2023b). As discussed in Section 4, the combination of both data sets allows us to derive an unimodal solution for the orbital period, independent of Gaia’s astrometric solution. The joint fit to all available RV data and the astrometry yields the most accurate solution thus far.

5.1. Comparison with Theoretical Predictions

Prior to Gaia DR3, several studies calculated the expected population of black holes with luminous companions that could be detected with Gaia. The predicted Gaia yields range from tens to thousands of such binaries by the end of the mission (Breivik et al. 2017; Mashian & Loeb 2017; Wiktorowicz et al. 2020; Chawla et al. 2022; Janssens et al. 2022; Shikauchi et al. 2022; Wang et al. 2022). Although the quality cuts on orbital solutions described by Halbwachs et al. (2022) may have removed more binary systems that contain black holes, the identification of only two confident black hole-luminous companion binaries in DR3 so far (see El-Badry et al. 2023a, as well as the earlier identification of this source by Tanikawa et al. (2023) in their analysis of Gaia data) suggests that the upper end of those predictions is likely to be too optimistic. The properties of Gaia DR3 4373465352415301632 are quite similar to the most common binary parameters predicted by, e.g., Breivik et al. (2017), Yalinewich et al. (2018), and Shao & Li (2019) in black hole mass, companion mass, period, semimajor axis, and apparent magnitude. The only deviation from those expectations is the eccentricity, where the observed value differs from the most likely values of $e < 0.1$ or (in the case of significant kick velocities) $e > 0.9$. In this section, we

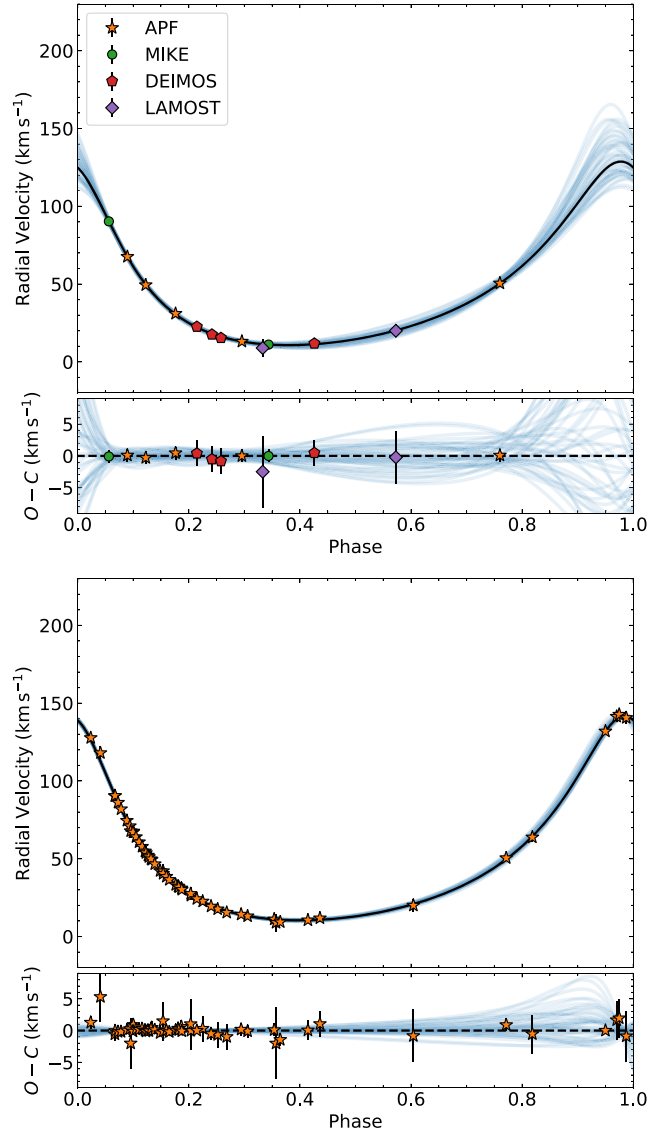


Figure 12. Phase-folded radial velocity curve for the data listed in Table 2 (top) and for all available data (bottom). The black line in the top panel represents the most likely orbit, and the light-blue curves illustrate a random selection of individual MCMC samples. The orbits shown in the top panel are restricted to periods between 175 and 195 days. The residuals, observed minus calculated, are shown in the lower panels. The agreement is within ~ 5 km s $^{-1}$ for all RV measurements, and all χ^2 values indicate satisfactory fits, with χ^2 per degree of freedom below 1 for both data sets.

speculate that the observed eccentricity of $e \sim 0.4$ may have resulted from a possible architecture of a hierarchical triple system. Stellar triples are a common architecture and can affect the dynamical evolution of the system (Tokovinin et al. 2006; Tokovinin & Moe 2020; Chakrabarti et al. 2022; Lennon et al. 2022; Vigna-Gómez et al. 2022).

5.2. Formation Scenarios

Although the characteristics of the Gaia DR3 4373465352415301632 binary system do not appear to be unusual with respect to population synthesis predictions for binaries detectable by Gaia, the particular combination of properties that we have determined may require fine-tuning to explain. To begin, the mass ratio of the system is quite large, $M_2/M_1 = 10.3 \pm 1.2$. Although some low-mass companions to

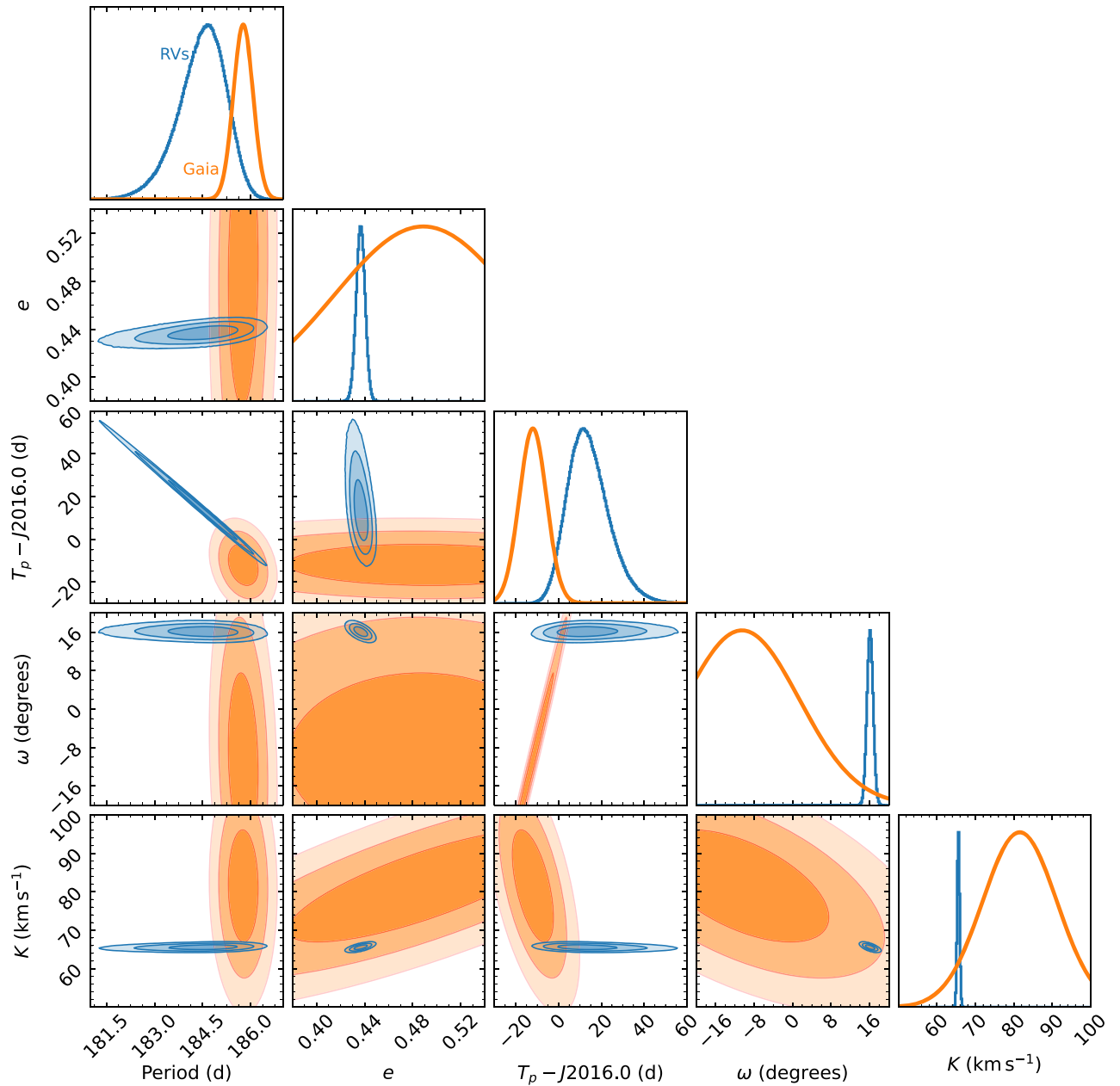


Figure 13. 1, 2, and 3σ confidence levels resulting from fits to all available RV data (blue contours), compared to the reported constraints from Gaia astrometry (orange contours). Although the RV data are qualitatively consistent with the Gaia astrometry, most orbital parameters show discrepancies at the $2\text{--}3\sigma$ level, even with the full RV data set. Since the χ^2 value for RV fits indicates that the velocity uncertainties have not been underestimated, we conclude that the Gaia errors must have been underestimated.

massive stars have been identified (e.g., GRAVITY Collaboration et al. 2018; Reggiani et al. 2022c), this does not seem to be the most common configuration for OB stars. The initial mass ratio of the system must have been even larger; for example, the initial-final mass relation of Raithel & Sukhbold (2018) suggests that a $\sim 10 M_{\odot}$ black hole would have had a zero-age main-sequence mass of $\sim 15\text{--}50 M_{\odot}$. Moreover, it is not clear that a binary with a separation of ~ 1 au should have survived the evolution of the massive component. Prior to the formation of the black hole, the orbit must have been tighter because of the mass that the system lost when the black hole formed. (If the black hole received a natal kick, then that also would have heated the system, further reducing the inferred initial separation.) The maximum radius reached by a $15\text{--}50 M_{\odot}$ star

after crossing the Hertzsprung gap is $\gtrsim 400 R_{\odot}$ (Martins & Palacios 2013), indicating that the system could not have avoided a common envelope phase unless the progenitor evolved quasi-homogeneously (e.g., Ramachandran et al. 2019; Gilkis et al. 2021; El-Badry et al. 2022b, suggesting that stars more massive than $\sim 30 M_{\odot}$ may evolve quasi-homogeneously without respect to rotation.) Depending on the duration of that period and on the common envelope ejection efficiency, a merger might be expected to follow, which makes the survival of the G star until the present surprising.

One way to avoid this conundrum is if the system was initially a triple, consisting of an inner binary orbited by the G star. Massive stars are often found with close massive companions (Sana et al. 2012), so there would be nothing

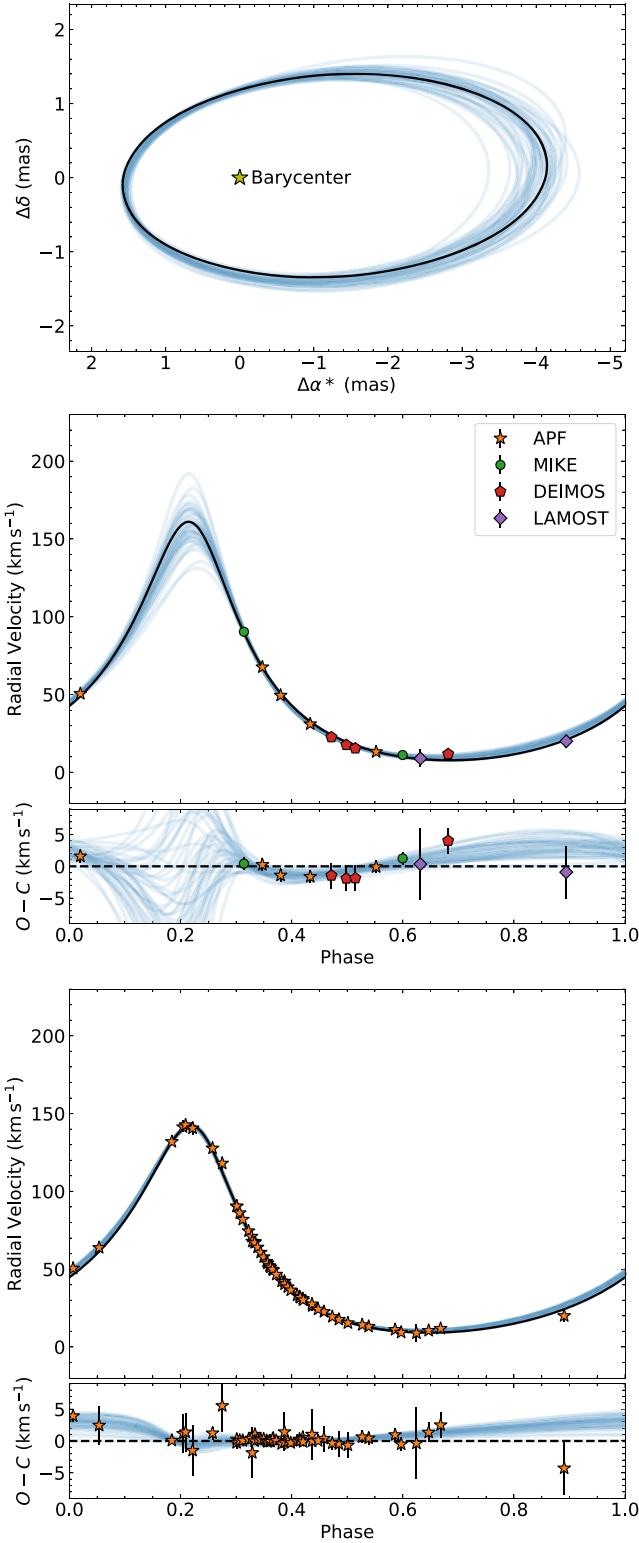


Figure 14. Joint orbital fit (see text for the description of the joint fit) to the astrometry (top) and radial velocities (middle) for the RV data set given in Table 2, and for all available radial velocity data (bottom). The black lines in the lower two panels show the steps in the RV chains that are most consistent with the Gaia astrometry. These orbits are in tension with the RVs. The light-blue points are drawn from weighted RV chains conditioned on the Gaia data as described in the text.

unusual about this architecture. Interactions between the two inner stars could then have proceeded either via mass loss or a merger in such a way as to prevent either star from expanding

enough to engulf their wider companion. The question posed by this scenario is whether the inner binary ultimately merged, either before or after the formation of the black hole. If so, then that merger could have resulted in the production of the $9.3 M_{\odot}$ black hole that we have identified. Meanwhile, if the stars did not merge, then an inner binary of two compact objects with a combined mass of $9.3 M_{\odot}$ could still be present. Many such combinations are possible, and of course this suggestion is entirely speculative at the moment, but a binary with a combined mass of $9.3 M_{\odot}$ would likely involve at least one object residing in the mass gap (e.g., Ö 1918), which would be of considerable interest. In the next section, we discuss whether there would be any observable consequences of the $9.3 M_{\odot}$ dark mass being subdivided into a binary.

5.3. A Third Companion?

We have investigated with `orvara` the possibility that Gaia DR3 4373465352415301632 may be a triple system containing two unseen companions, but our present data set does not allow us to constrain the posterior distributions of a hierarchical triple. Extended radial velocity monitoring could make it possible to study the rich dynamics of a triple system, and we briefly speculate here on some of the possibilities that could be directly observed. Although the incidence of triples drops dramatically for periods greater than ~ 10 days (Tokovinin et al. 2006; Tokovinin & Moe 2020), compact triple systems are not uncommon, and there is indeed a population of compact triples that manifest large eclipse transit variations in eclipsing binaries (Borkovits et al. 2015). Here, we focus on the more likely possibility of a compact inner binary with the G star as part of the outer system (Section 5.2). A similar scenario has been investigated in El-Badry et al. (2023b).

If this indeed is a hierarchical triple system, then the Kozai–Lidov mechanism would allow for an exchange between the eccentricity and the inclination (Chang 2009; Naoz et al. 2013; Suzuki et al. 2019). The Kozai–Lidov timescale (Antognini 2015), t_{KL} , is given by:

$$t_{\text{KL}} \sim P_{\text{in}} \frac{m_1 + m_2}{m_3} \left(\frac{a_{\text{out}}}{a_{\text{in}}} \right)^3 (1 - e_{\text{out}}^2)^{3/2}, \quad (3)$$

where P_{in} is the orbital period of the inner binary, a_{out} and a_{in} are the semimajor axes of the outer and inner systems, e_{out} is the eccentricity of the outer system, and the masses of the three bodies are given by m_1 , m_2 , and m_3 . For our specific case here, if we consider an inner binary of combined mass $m_1 + m_2 \sim 9.3 M_{\odot}$ that has a third body with a semimajor axis that is 3(10) times that of the inner binary, then this gives a Kozai–Lidov timescale of $\sim 100(5000)$ yr. However, the shift in the velocity is $\sim 10^{-2}(10^{-4})$ per orbital period. For this specific case, the velocity change in physical units translates to $\sim 1000(10)$ m s^{-1} per orbit, which could in principle be observed, especially if the inner binary is not too close. This effect (the osculation of the orbit of the inner binary due to the Kozai–Lidov effect) is modified by a general relativistic correction term (Anderson et al. 2017). This is likely to be the dominant dynamical effect beyond that of Keplerian motion. Other dynamical effects for binary systems recently reviewed by Chakrabarti et al. (2022; including tidal effects and the general relativistic precession) are subdominant to this

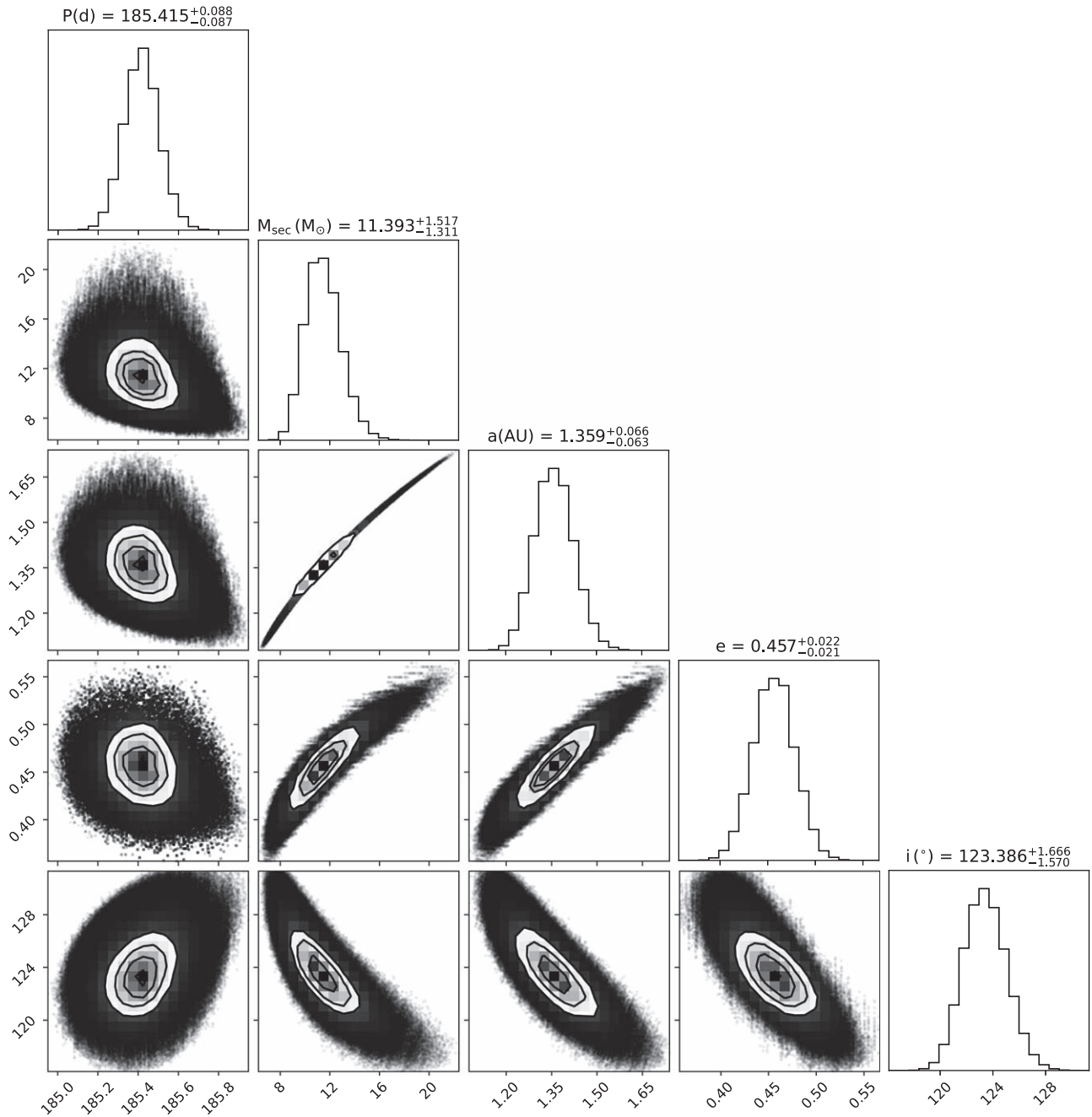


Figure 15. Posterior distributions from our joints fits to our velocity data and LAMOST data (as listed in Table 2), and Gaia astrometry. The parameter constraints are tighter and correlations are reduced compared to the fit to the velocities alone.

signal. Thus, the effects of the Kozai–Lidov effect may become manifest over several orbital periods for this system, even for a widely separated hierarchical system. In this context, it is advantageous that the companion star is a G star, with spectra that indicate that it has low stellar jitter (Wright 2005). For stars with low stellar jitter, high precision measurements should be able to capture this effect.

5.4. Comparison with 2MASS J05215658 + 4359220

Earlier work on the report of the black hole binary system with a noninteracting giant companion by Thompson et al. (2019) indicated an unusually high [C/N] abundance ratio for

its mass and evolutionary state. If the mass inferred for the red giant is correct, then this abundance pattern may have resulted from previous interaction with the black hole progenitor star (we note that van den Heuvel & Tauris (2020) argue that if the red giant’s mass is $\sim 1M_{\odot}$, then the companion could be a binary with two main-sequence stars). Low-mass X-ray binaries with black hole companions are also found to be metal-rich, with large abundances of α elements (Casares et al. 2017). For Gaia DR3 4373465352415301632, a comparison with synthetic spectra indicates an approximately solar [C/N] ratio, as expected for a main-sequence star of its metallicity. The [C/N] ratio of Gaia DR3 4373465352415301632 places it in the typical observed locus of main-sequence stars

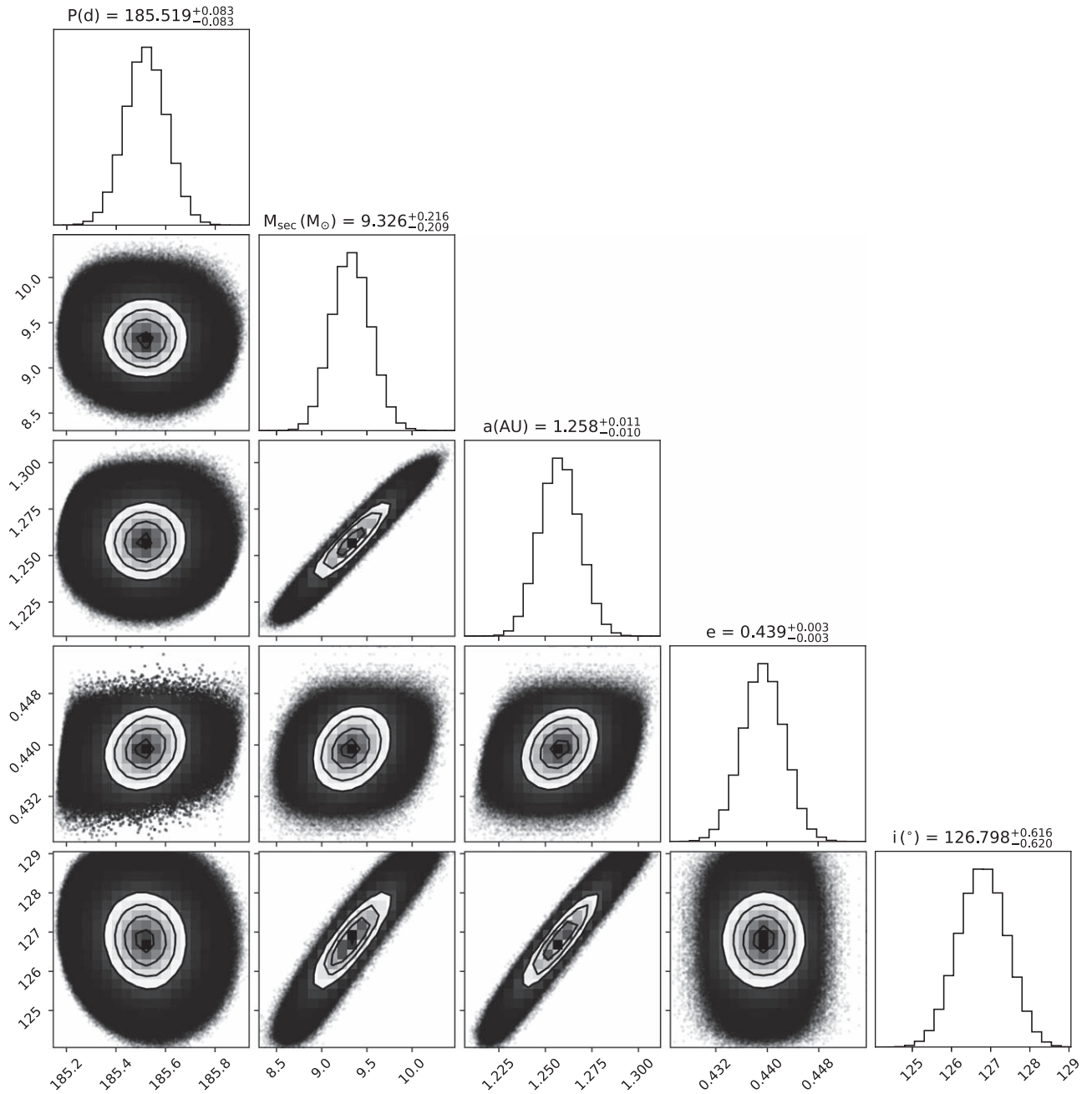


Figure 16. Posterior distributions from our joints fits to all available velocity data (including RV data from El-Badry et al. 2023) and Gaia astrometry. The parameter constraints are tighter and correlations are reduced compared to the fit to the velocities alone.

(Pinsonneault et al. 2018), which is consistent with its small Roche lobe to semimajor axis ratio. We find that the Roche limit to the semimajor axis for the G star is 0.2, which indicates that it is stable against tidal disintegration.

5.5. Estimate for the Number of Systems in the Galaxy

Given the current uncertainty in the formulation of the common envelope channel, we adopt a simpler approach and estimate the number of such systems that may exist in the galaxy. Here, we do not consider binary (and triple) evolution effects, which may be more significant than IMF dependencies.

We assume a Salpeter IMF:

$$\frac{dn}{dm} = \mathcal{N}m^{-2.35}, \quad (4)$$

where dn/dm is the number of stars per mass bin, and the normalization, \mathcal{N} , can be set by integrating the number of stars per mass bin over the limits of the masses of stars in the Salpeter IMF, i.e., where $m_{\min} = 0.1 M_{\odot}$ and $m_{\max} = 100 M_{\odot}$ are the upper and lower limits, and equating to the observed number of stars in the galaxy, N_{*} . The binary fraction of high-mass stars is nearly unity ($f_b \sim 1$) (Sana et al. 2009; Maíz Apellániz et al. 2016) and the companion masses, m_c , are taken

from a flat distribution in mass ratio, $q = m_c/m$, e.g., $dP/dq = 1$ (Sana et al. 2012; Chulkov 2021).

$$N = f_b \mathcal{N} \int_{m_{\text{lower}}}^{m_{\text{max}}} \frac{dn}{dm} dm \int_{q_1}^{q_2} \frac{dP}{dq} dq$$

$$= 0.42 f_b \mathcal{N} (m_{\text{lower}}^{-2.35} - m_{\text{max}}^{-2.35}) (m_2 - m_1) \quad (5)$$

where m_{lower} is the minimum progenitor mass required to form a $\sim 10 M_{\odot}$ black hole, which we take to be $\sim 20 M_{\odot}$ (Sukhbold et al. 2016); and m_1 and m_2 are the lower and upper mass range of zero-age main-sequence masses of G-type stars, which we take to be $0.8 M_{\odot}$ and $1.2 M_{\odot}$, respectively. This gives a total number of binaries of $\sim 8 \times 10^5$, which is comparable to the number of binaries with a black hole and a luminous companion in the zero-kick model by Breivik et al. (2017).

5.6. Milky Way Orbit

We integrate the orbit of Gaia DR3 43734653 52415301632 backwards in time 500 Myr in the Galactic potential, as shown in Figure 17. Here, we use the potential derived from accelerations measured directly from pulsar timing (Chakrabarti et al. 2021), which provides the most direct probe of the Galactic mass distribution. Using potentials derived from kinematic assumptions (e.g., Bovy 2015) produces similar results to within a factor of ~ 2 . The star remains confined within a few hundred pc of the Galactic plane at all times, confirming that it formed as part of the thin disk population. Unless the natal kick of the black hole happened to be oriented within the disk of the galaxy, then the low scale height of the orbit indicates that the kick velocity must have been small. Given the low scale height of the orbit, ~ 0.4 kpc, the vertical kick velocity is of order $\sim 10 \text{ km s}^{-1}$. This is similar to the negligible kick velocities for Cyg X-1 and VFTS 243 (Mirabel & Rodrigues 2003; Shenar et al. 2022). The orbit of Gaia DR3 4373465352415301632 around the Milky Way is somewhat eccentric, with a pericenter of ~ 7 kpc and apocenter of ~ 12 kpc, reaching substantially larger distances than the Sun does, which is consistent with its older age.

6. Conclusion

A summary of our main results follows:

1. We searched the Gaia DR3 binary catalog to identify possible black hole companions to main-sequence stars. We identified Gaia DR3 4373465352415301632 as a particularly interesting source on the basis of its large mass ratio and location near the Gaia main sequence.
2. Fitting the SED of Gaia DR3 4373465352415301632 with single stellar atmosphere models, we find that the photometry is consistent with a modestly metal-poor G star on the main sequence. Adding a second source does not substantially improve the quality of the SED fits, which indicates that there is no evidence for the presence of more than one luminous star.
3. We determine stellar parameters from a high-resolution spectrum, finding $T_{\text{eff}} = 5972 \pm 100 \text{ K}$, $\log g = 4.54 \pm 0.15$, $[\text{Fe}/\text{H}] = -0.30 \pm 0.10$, $M = 0.91 \pm 0.10 M_{\odot}$, and age = $7.1 \pm 3.8 \text{ Gyr}$, which are generally in good agreement with those inferred from the SED. The chemical abundance pattern shows no abnormalities when

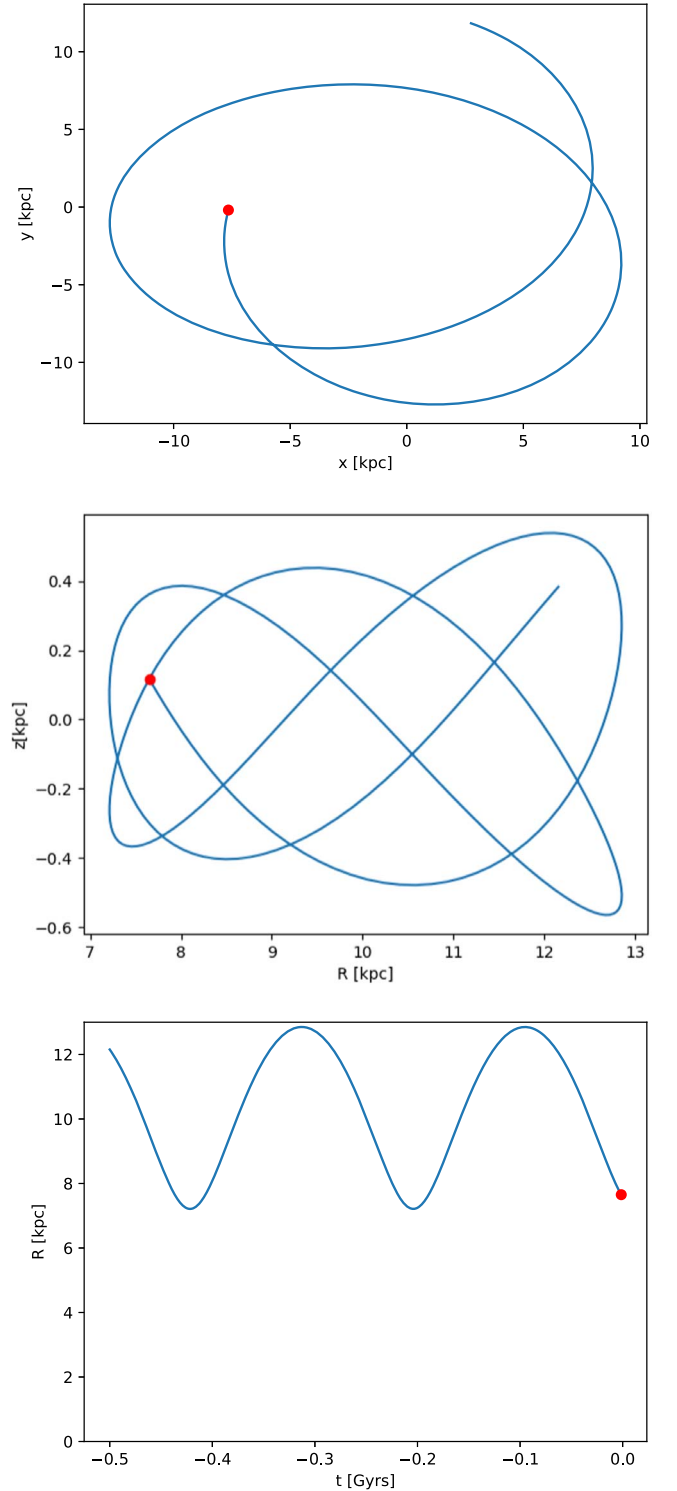


Figure 17. Orbit in the galaxy, integrated backwards from present day for 500 Myr; the red dot marks the present day ($t = 0$).

4. We have carried out follow-up radial velocity observations for this source over the four months from its discovery until it went into conjunction with the Sun, and our fits to the velocities give an orbital period of $184.28^{+0.75}_{-0.89} \text{ d}$, an eccentricity of $0.411^{+0.034}_{-0.021}$, and a velocity semi-amplitude of $60.6^{+10.0}_{-5.8} \text{ km s}^{-1}$. The radial

velocity curve predicted from the astrometric orbital solution is in reasonable agreement with the data, which confirms that the Gaia orbit is not spurious. We then computed joint fits to the astrometric data and the RVs, which (including the RV measurements from El-Badry et al. 2023b) give a companion mass of $9.326^{+0.216}_{-0.209} M_{\odot}$, an orbital period of $185.52^{+0.08}_{-0.08}$ day, an eccentricity of $0.439^{+0.0036}_{-0.0030}$, a semimajor axis of $1.258^{+0.010}_{-0.011}$ au, and an inclination of 126.79 ± 0.62 .

5. The fit to all available RV data gives a best-fit χ^2 of 24 for 52 total radial velocity measurements and six free parameters (46 degrees of freedom). This low χ^2 value indicates that the RV errors and our derived parameter uncertainties may be overestimated. However, there is $\sim 2\sigma$ disagreement between the best-fit parameters from the RVs and the Gaia astrometry. The 1σ confidence intervals overlap only for the eccentricity. For our joint fits to the astrometry and RV data, we find that when we condition the RV fits on the Gaia data, the increase in χ^2 is a factor of four greater than what is expected. This suggests the Gaia uncertainties have been underestimated by a factor of ≈ 2 .
6. Given the combination of the large mass of the dark companion and a semimajor axis of Gaia DR3 4373465352415301632 that is neither very large nor very small, the formation channel for this system is not immediately clear. However, the most natural scenario may be that the visible G star was originally the outer tertiary component orbiting a close inner binary with two massive stars. A similar possibility is also discussed in El-Badry et al. (2023b).
7. The orbit of this system in the galaxy is consistent with that of thin disk stars, and the low scale height of the integrated Galactic orbit indicates that the kick velocity must have been small. At a distance of 468 ± 4 pc after correcting for the DR3 parallax bias (Lindgren et al. 2021a), as discussed by El-Badry et al. (2023b), Gaia DR3 4373465352415301632 is closer to the Sun than any black hole X-ray binaries with known distances (Corral-Santana et al. 2016) or any of the black holes identified through other techniques (Thompson et al. 2019; Lam et al. 2022; Sahu et al. 2022).
8. Discoveries of black holes around luminous stars from their measured accelerations now provide a new avenue for understanding the formation channels of black holes in the galaxy. Simple estimates suggest that there are $\sim 10^6$ similar systems in the Milky Way. Although our current data cannot constrain the possibility that Gaia DR3 4373465352415301632 is actually a triple, future RV monitoring may enable us to witness the rich dynamics that can be manifest in hierarchical triple systems.

Acknowledgments

We thank the anonymous referee for a thorough review that helped to improve this paper. We are grateful to Mirek Brandt for helpful discussions on `orvara`, Adrian Price-Whelan for assistance with *The Joker*, Brad Holden for his help with APF data and observations, Lieke van Son for discussion of binary evolution, and Alex Ji for advice on MIKE data handling in Python. S.C. also acknowledges support from NSF AAG 2009828 and from the RCSA time domain astrophysics program.

This work has made use of data from the European Space Agency (ESA) mission Gaia (<https://www.cosmos.esa.int/gaia>), processed by the Gaia Data Processing and Analysis Consortium (DPAC, <https://www.cosmos.esa.int/web/gaia/dpac/consortium>). Funding for the DPAC has been provided by national institutions, in particular the institutions participating in the Gaia Multilateral Agreement.

This paper includes data gathered with the 6.5 m Magellan Telescopes located at Las Campanas Observatory, Chile.

Some of the data presented herein were obtained at the W. M. Keck Observatory, which is operated as a scientific partnership among the California Institute of Technology, the University of California and the National Aeronautics and Space Administration. The Observatory was made possible by the generous financial support of the W. M. Keck Foundation. The authors wish to recognize and acknowledge the very significant cultural role and reverence that the summit of Maunakea has always had within the indigenous Hawaiian community. We are most fortunate to have the opportunity to conduct observations from this mountain.

Guoshoujing Telescope (the Large Sky Area Multi-Object Fiber Spectroscopic Telescope LAMOST) is a National Major Scientific Project built by the Chinese Academy of Sciences. Funding for the project has been provided by the National Development and Reform Commission. LAMOST is operated and managed by the National Astronomical Observatories, Chinese Academy of Sciences.

This research has made use of NASA's Astrophysics Data System Bibliographic Services.

Facilities: Gaia, Magellan:II (MIKE), Automated Planet Finder (Levy), Keck:II (DEIMOS).

Software: ARIADNE (Vines & Jenkins 2022), SpecMatch-Emp (Yee et al. 2017), smhr (Casey 2014), isochrones (Morton 2015), MultiNest (Feroz & Hobson 2008; Feroz et al. 2009, 2019), PyMultiNest (Buchner et al. 2014), MOOG (Snedden 1973), `orvara` (Brandt et al. 2021), *The Joker* (Price-Whelan et al. 2017), `exoplanet` (Foreman-Mackey et al. 2021a, 2021b)

ORCID iDs

Sukanya Chakrabarti  <https://orcid.org/0000-0001-6711-8140>

Joshua D. Simon  <https://orcid.org/0000-0002-4733-4994>

Peter A. Craig  <https://orcid.org/0000-0002-3673-0668>

Henrique Reggiani  <https://orcid.org/0000-0001-6533-6179>

Timothy D. Brandt  <https://orcid.org/0000-0003-2630-8073>

Puragra Guhathakurta  <https://orcid.org/0000-0001-8867-4234>

Paul A. Dalba  <https://orcid.org/0000-0002-4297-5506>

Evan N. Kirby  <https://orcid.org/0000-0001-6196-5162>

Philip Chang  <https://orcid.org/0000-0002-2137-2837>

Daniel R. Hey  <https://orcid.org/0000-0003-3244-5357>

Alessandro Savino  <https://orcid.org/0000-0002-1445-4877>

Marla Geha  <https://orcid.org/0000-0002-7007-9725>

References

- Abbott, B. P., Abbott, R., Abbott, T. D., et al. 2016, *PhRvD*, 93, 122003
 Abbott, B. P., Abbott, R., Abbott, T. D., et al. 2019, *ApJL*, 882, L24
 Abbott, R., Abbott, T. D., Abraham, S., et al. 2021, *PhRvX*, 11, 021053
 Abdul-Masih, M., Banyard, G., Bodensteiner, J., et al. 2020, *Natur*, 580, E11
 Ahumada, R., Prieto, C. A., Almeida, A., et al. 2020, *ApJS*, 249, 3
 Amarsi, A. M., & Asplund, M. 2017, *MNRAS*, 464, 264

- Amarsi, A. M., Lind, K., Asplund, M., Barklem, P. S., & Collet, R. 2016, *MNRAS*, **463**, 1518
- Amarsi, A. M., Lind, K., Osorio, Y., et al. 2020, *A&A*, **642**, A62
- Amarsi, A. M., Nissen, P. E., & Skúladóttir, A. 2019, *A&A*, **630**, A104
- Anderson, K. R., Lai, D., & Storch, N. I. 2017, *MNRAS*, **467**, 3066
- Andrews, J. J., Taggart, K., & Foley, R. 2022, arXiv:2207.00680
- Antognini, J. M. O. 2015, *MNRAS*, **452**, 3610
- Antonini, F., & Rasio, F. A. 2016, *ApJ*, **831**, 187
- Asplund, M., Amarsi, A. M., & Grevesse, N. 2021, *A&A*, **653**, A141
- Bavera, S. S., Fragos, T., Qin, Y., et al. 2020, *A&A*, **635**, A97
- Belczynski, K., Holz, D. E., Bulik, T., & O'Shaughnessy, R. 2016, *Natur*, **534**, 512
- Berg, D. A., Pogge, R. W., Skillman, E. D., et al. 2020, *ApJ*, **893**, 96
- Bernstein, R., Shtetman, S. A., & Gunnels, S. M. 2003, *Proc. SPIE*, **4841**, 1694
- Binnendijk, L. 1960, *Properties of Double Stars; a Survey of Parallaxes and Orbits* (Philadelphia, PA: Univ. Pennsylvania Press)
- Blackwell-Whitehead, R. J., Toner, A., Hibbert, A., Webb, J., & Ivarsson, S. 2005, *MNRAS*, **364**, 705
- Bodensteiner, J., Shenar, T., Mahy, L., et al. 2020, *A&A*, **641**, A43
- Borkovits, T., Rappaport, S., Hajdu, T., & Sztakovics, J. 2015, *MNRAS*, **448**, 946
- Bovy, J. 2015, *ApJS*, **216**, 29
- Brandt, T. D., Dupuy, T. J., Li, Y., et al. 2021, *AJ*, **162**, 186
- Breivik, K., Chatterjee, S., & Larson, S. L. 2017, *ApJL*, **850**, L13
- Bresolin, F., Kennicutt, R. C., & Ryan-Weber, E. 2012, *ApJ*, **750**, 122
- Brewer, J. M., Fischer, D. A., Valenti, J. A., & Piskunov, N. 2016, *ApJS*, **225**, 32
- Buchner, J., Georgakakis, A., Nandra, K., et al. 2014, *A&A*, **564**, A125
- Butler, R. P., Marcy, G. W., Williams, E., et al. 1996, *PASP*, **108**, 500
- Capitanio, L., Lallement, R., Vergely, J. L., Elyajouri, M., & Monreal-Ibero, A. 2017, *A&A*, **606**, A65
- Casares, J., Jonker, P. G., Israelian, G., et al. 2017, in *Handbook of Supernovae*, ed. A. W. Alsabti & P. Murdin (Berlin: Springer), 1499
- Casey, A. R. 2014, PhD thesis, Australian National Univ., Canberra
- Castelli, F., & Kurucz, R. L. 2003, in *IAU Symp. 210, Modelling of Stellar Atmospheres*, ed. N. Piskunov, W. W. Weiss, & D. F. Gray (San Francisco, CA: ASP), A20
- Chakrabarti, S., Chang, P., Lam, M. T., Vigeland, S. J., & Quillen, A. C. 2021, *ApJL*, **907**, L26
- Chakrabarti, S., Chang, P., O'Shaughnessy, R., et al. 2017, *ApJL*, **850**, L4
- Chakrabarti, S., Dell, B., Graur, O., et al. 2018, *ApJL*, **863**, L1
- Chakrabarti, S., Stevens, D. J., Wright, J., et al. 2022, *ApJL*, **928**, L17
- Chang, P. 2009, *MNRAS*, **393**, 224
- Chawla, C., Chatterjee, S., Breivik, K., et al. 2022, *ApJ*, **931**, 107
- Choi, J., Dotter, A., Conroy, C., et al. 2016, *ApJ*, **823**, 102
- Chubak, C., Marcy, G., Fischer, D. A., et al. 2012, arXiv:1207.6212
- Chulkov, D. 2021, *MNRAS*, **501**, 769
- Cooper, M. C., Newman, J. A., Davis, M., Finkbeiner, D. P., & Gerke, B. F. 2012, spec2d: DEEP2 DEIMOS Spectral Pipeline, Astrophysics Source Code Library, record, ascl:1203.003
- Corral-Santana, J. M., Casares, J., Muñoz-Darias, T., et al. 2013, *Sci*, **339**, 1048
- Corral-Santana, J. M., Casares, J., Muñoz-Darias, T., et al. 2016, *A&A*, **587**, A61
- Cui, X.-Q., Zhao, Y.-H., Chu, Y.-Q., et al. 2012, *RAA*, **12**, 1197
- Cutri, R. M., Skrutskie, M. F., van Dyk, S., et al. 2003, 2MASS All Sky Catalog of point sources
- Cutri, R. M., Wright, E. L., Conrow, T., et al. 2021, *yCat*, **II/328**
- de Mink, S. E., & Mandel, I. 2016, *MNRAS*, **460**, 3545
- El-Badry, K., & Burdge, K. B. 2022, *MNRAS*, **511**, 24
- El-Badry, K., Burdge, K. B., & Mróz, P. 2022a, *MNRAS*, **511**, 3089
- El-Badry, K., Conroy, C., Fuller, J., et al. 2022b, *MNRAS*, **517**, 4916
- El-Badry, K., & Quataert, E. 2020, *MNRAS*, **493**, L22
- El-Badry, K., & Quataert, E. 2021, *MNRAS*, **502**, 3436
- El-Badry, K., & Rix, H.-W. 2022, *MNRAS*, **515**, 1266
- El-Badry, K., Rix, H.-W., Cendes, Y., et al. 2023a, *MNRAS*, **521**, 4323
- El-Badry, K., Rix, H.-W., Quataert, E., et al. 2023b, *MNRAS*, **518**, 1057
- El-Badry, K., Seeburger, R., Jayasinghe, T., et al. 2022c, *MNRAS*, **512**, 5620
- Eldridge, J. J., Stanway, E. R., Breivik, K., et al. 2020, *MNRAS*, **495**, 2786
- Faber, S. M., Phillips, A. C., Kibrick, R. I., et al. 2003, *Proc. SPIE*, **4841**, 1657
- Feroz, F., & Hobson, M. P. 2008, *MNRAS*, **384**, 449
- Feroz, F., Hobson, M. P., & Bridges, M. 2009, *MNRAS*, **398**, 1601
- Feroz, F., Hobson, M. P., Cameron, E., & Pettitt, A. N. 2019, *OJAp*, **2**, 10
- Fitzpatrick, E. L. 1999, *PASP*, **111**, 63
- Flewelling, H. A., Magnier, E. A., Chambers, K. C., et al. 2020, *ApJS*, **251**, 7
- Foreman-Mackey, D., Luger, R., Agol, E., et al. 2021a, *JOSS*, **6**, 3285
- Foreman-Mackey, D., Luger, R., Agol, E., et al. 2021b, exoplanet: Gradient-based probabilistic inference for exoplanet data & other astronomical time series, v0.5.1, Zenodo, doi 10.5281/zenodo.1998447
- Frost, A. J., Bodensteiner, J., Rivinius, T., et al. 2022, *A&A*, **659**, L3
- Fukugita, M., Ichikawa, T., Gunn, J. E., et al. 1996, *AJ*, **111**, 1748
- Fulton, B. J., Weiss, L. M., Sinukoff, E., et al. 2015, *ApJ*, **805**, 175
- Gaia Collaboration, Arenou, F., Babusiaux, C., et al. 2022a, arXiv:2206.05595
- GRAVITY Collaboration, Vallenari, A., Brown, A. G. A., et al. 2022b, arXiv:2208.00211
- Gaia Collaboration, Prusti, T., de Bruijne, J. H. J., et al. 2016, *A&A*, **595**, A1
- Gao, S., Liu, C., Zhang, X., et al. 2014, *ApJL*, **788**, L37
- Giesers, B., Dreizler, S., Husser, T.-O., et al. 2018, *MNRAS*, **475**, L15
- Giesers, B., Kamann, S., Dreizler, S., et al. 2019, *A&A*, **632**, A3
- Gilkis, A., Shenar, T., Ramachandran, V., et al. 2021, *MNRAS*, **503**, 1884
- González Hernández, J. I., Rebolo, R., Israelian, G., et al. 2008, *ApJ*, **679**, 732
- GRAVITY Collaboration, Karl, M., Pfuhl, O., et al. 2018, *A&A*, **620**, A116
- Gray, R. O., & Corbally 2009, *Stellar Spectral Classification* (Princeton, NJ: Princeton Univ. Press)
- Gray, R. O., Corbally, C. J., Garrison, R. F., McFadden, M. T., & Robinson, P. E. 2003, *AJ*, **126**, 2048
- Halbwachs, J.-L., Pourbaix, D., Arenou, F., et al. 2022, arXiv:2206.05726
- Henden, A. A. 2019, *JAAVSO*, **47**, 130
- Henden, A. A., Templeton, M., Terrell, D., et al. 2016, *yCat*, **II/336**
- Holl, B., Sozzetti, A., Sahlmann, J., et al. 2022, arXiv:2206.05439
- Howard, A. W., Johnson, J. A., Marcy, G. W., et al. 2010, *ApJ*, **721**, 1467
- Husser, T. O., Wende-von Berg, S., Dreizler, S., et al. 2013, *A&A*, **553**, A6
- Janssens, S., Shenar, T., Sana, H., et al. 2022, *A&A*, **658**, A129
- Jayasinghe, T., Stanek, K. Z., Thompson, T. A., et al. 2021, *MNRAS*, **504**, 2577
- Jayasinghe, T., Thompson, T. A., Kochanek, C. S., et al. 2022, *MNRAS*, **516**, 5945
- Ji, A. P., Li, T. S., Simon, J. D., et al. 2020, *ApJ*, **889**, 27
- Kelson, D. D. 2003, *PASP*, **115**, 688
- Kennicutt, Robert C., & Bresolin, J. 2003, *ApJ*, **591**, 801
- Kirby, E. N., Simon, J. D., & Cohen, J. G. 2015, *ApJ*, **810**, 56
- Kobayashi, C., Karakas, A. I., & Lugaro, M. 2020, *ApJ*, **900**, 179
- Lallement, R., Capitanio, L., Ruiz-Dern, L., et al. 2018, *A&A*, **616**, A132
- Lallement, R., Vergely, J. L., Valette, B., et al. 2014, *A&A*, **561**, A91
- Lam, C. Y., Lu, J. R., Udalski, A., et al. 2022, *ApJL*, **933**, L23
- Lamberts, A., Garrison-Kimmel, S., Clausen, D. R., & Hopkins, P. F. 2016, *MNRAS*, **463**, L31
- Lehmer, B. D., Eufrazio, R. T., Basu-Zych, A., et al. 2021, *ApJ*, **907**, 17
- Lejeune, T., Cuisinier, F., & Buser, R. 1997, *A&AS*, **125**, 229
- Lejeune, T., Cuisinier, F., & Buser, R. 1998, *A&AS*, **130**, 65
- Lennon, D. J., Dufton, P. L., Villaseñor, J. I., et al. 2022, *A&A*, **665**, A180
- Lind, K., Asplund, M., Barklem, P. S., & Belyaev, A. K. 2011, *A&A*, **528**, A103
- Lindgren, L., Bastian, U., Biermann, M., et al. 2021a, *A&A*, **649**, A4
- Lindgren, L., Klioner, S. A., Hernández, J., et al. 2021b, *A&A*, **649**, A2
- Lipartito, I., Bailey, John, I., & Brandt, I. 2021, *AJ*, **162**, 285
- Liu, J., Zhang, H., Howard, A. W., et al. 2019, *Natur*, **575**, 618
- Luo, A. L., Zhao, Y. H., Zhao, G., et al. 2022, *yCat*, **V/156**
- Mahy, L., Sana, H., Shenar, T., et al. 2022, *A&A*, **664**, A159
- Maíz Apellániz, J., Sota, A., Arias, J. I., et al. 2016, *ApJS*, **224**, 4
- Marchant, P., Pappas, K. M. W., Gallegos-García, M., et al. 2021, *A&A*, **650**, A107
- Martin, D. C., Fanson, J., Schiminovich, D., et al. 2005, *ApJL*, **619**, L1
- Martins, F., & Palacios, A. 2013, *A&A*, **560**, A16
- Mashian, N., & Loeb, A. 2017, *MNRAS*, **470**, 2611
- McWilliam, A. 1998, *AJ*, **115**, 1640
- Meléndez, J., Schirbel, L., Monroe, T. R., et al. 2014, *A&A*, **567**, L3
- Mirabel, I. F., & Rodrigues, I. 2003, *Sci*, **300**, 1119
- Moe, M., Kratter, K. M., & Badenes, C. 2019, *ApJ*, **875**, 61
- Morrissey, P., Conrow, T., Barlow, T. A., et al. 2007, *ApJS*, **173**, 682
- Morton, T. D. 2015, *isochrones: Stellar model grid package*
- Naoz, S., Farr, W. M., Lithwick, Y., Rasio, F. A., & Teyssandier, J. 2013, *MNRAS*, **431**, 2155
- Neijssel, C. J., Vigna-Gómez, A., Stevenson, S., et al. 2019, *MNRAS*, **490**, 3740
- Newman, J. A., Cooper, M. C., Davis, M., et al. 2013, *ApJS*, **208**, 5
- Olejak, A., Belczynski, K., Bulik, T., & Sobolewska, M. 2020, *A&A*, **638**, A94
- Onken, C. A., Wolf, C., Bessell, M. S., et al. 2019, *PASA*, **36**, e033
- Orosz, J. A., Kuulkers, E., van der Klis, M., et al. 2001, *ApJ*, **555**, 489
- Özel, F., Psaltis, D., Narayan, R., & McClintock, J. E. 2010, *ApJ*, **725**, 1918

- Panizo-Espinar, G., Armas Padilla, M., Muñoz-Darias, T., et al. 2022, *A&A*, **664**, A100
- Pinsonneault, M. H., Elsworth, Y. P., Tayar, J., et al. 2018, *ApJS*, **239**, 32
- Price-Whelan, A. M., Hogg, D. W., Foreman-Mackey, D., & Rix, H.-W. 2017, *ApJ*, **837**, 20
- Prochaska, J. X., & McWilliam, A. 2000, *ApJL*, **537**, L57
- Prochaska, J. X., Naumov, S. O., Carney, B. W., McWilliam, A., & Wolfe, A. M. 2000, *AJ*, **120**, 2513
- Radovan, M. V., Cabak, G. F., Laiterman, L. H., Lockwood, C. T., & Vogt, S. S. 2010, *Proc. SPIE*, **7735**, 77354K
- Raithel, C. A., & Sukhbold, T. 2018, *ApJ*, **856**, 35
- Ramachandran, V., Hamann, W. R., Oskina, L. M., et al. 2019, *A&A*, **625**, A104
- Reggiani, H., Amarsi, A. M., Lind, K., et al. 2019, *A&A*, **627**, A177
- Reggiani, H., Ji, A. P., Schlafman, K. C., et al. 2022a, *AJ*, **163**, 252
- Reggiani, H., & Meléndez, J. 2018, *MNRAS*, **475**, 3502
- Reggiani, H., Schlafman, K. C., Healy, B. F., Lothringer, J. D., & Sing, D. K. 2022b, *AJ*, **163**, 159
- Reggiani, M., Rainot, A., Sana, H., et al. 2022c, *A&A*, **660**, A122
- Riello, M., De Angeli, F., Evans, D. W., et al. 2021, *A&A*, **649**, A3
- Rivinius, T., Baade, D., Hadrava, P., Heida, M., & Klement, R. 2020, *A&A*, **637**, L3
- Russell, T. D., Del Santo, M., Marino, A., et al. 2022, *MNRAS*, **513**, 6196
- Sahu, K. C., Anderson, J., Casertano, S., et al. 2022, *ApJ*, **933**, 83
- Sana, H., de Mink, S. E., de Koter, A., et al. 2012, *Sci*, **337**, 444
- Sana, H., Gosset, E., & Evans, C. J. 2009, *MNRAS*, **400**, 1479
- Saracino, S., Kamann, S., Guarcello, M. G., et al. 2022, *MNRAS*, **511**, 2914
- Shahaf, S., Bashi, D., Mazeh, T., et al. 2023, *MNRAS*, **518**, 2991
- Shao, Y., & Li, X.-D. 2019, *ApJ*, **885**, 151
- Shenar, T., Bodensteiner, J., Abdul-Masih, M., et al. 2020, *A&A*, **639**, L6
- Shenar, T., Sana, H., Mahy, L., et al. 2022, *NatAs*, **6**, 1085
- Shikauchi, M., Tanikawa, A., & Kawanaka, N. 2022, *ApJ*, **928**, 13
- Simon, J. D., & Geha, M. 2007, *ApJ*, **670**, 313
- Simon, J. D., Li, T. S., Drlica-Wagner, A., et al. 2017, *ApJ*, **838**, 11
- Skrutskie, M. F., Cutri, R. M., Stiening, R., et al. 2006, *AJ*, **131**, 1163
- Snedden, C. A. 1973, PhD thesis, Univ. Texas at Austin
- Sohn, S. T., Majewski, S. R., Muñoz, R. R., et al. 2007, *ApJ*, **663**, 960
- Soubiran, C., Jasniewicz, G., Chemin, L., et al. 2018, *A&A*, **616**, A7
- Stefanik, R. P., Latham, D. W., & Torres, G. 1999, in ASP Conf. Ser. 185, IAU Colloq. 170: Precise Stellar Radial Velocities, ed. J. B. Hearnshaw & C. D. Scarfè (San Francisco, CA: ASP), 354
- Suárez-Andrés, L., González Hernández, J. I., Israelian, G., Casares, J., & Rebolo, R. 2015, *MNRAS*, **447**, 2261
- Sukhbold, T., Ertl, T., Woosley, S. E., Brown, J. M., & Janka, H. T. 2016, *ApJ*, **821**, 38
- Suzuki, H., Gupta, P., & Okawa, H. 2019, *MNRAS*, **486**, L52
- Tanikawa, A., Hattori, K., Kawanaka, N., et al. 2023, *ApJ*, **946**, 79
- Thompson, T. A., Kochanek, C. S., Stanek, K. Z., et al. 2019, *Sci*, **366**, 637
- Tokovinin, A., & Moe, M. 2020, *MNRAS*, **491**, 5158
- Tokovinin, A., Thomas, S., Sterzik, M., & Udry, S. 2006, *A&A*, **450**, 681
- Tonry, J. L., Stubbs, C. W., Lykke, K. R., et al. 2012, *ApJ*, **750**, 99
- van den Heuvel, E. P. J., Portegies Zwart, S. F., & de Mink, S. E. 2017, *MNRAS*, **471**, 4256
- van den Heuvel, E. P. J., & Tauris, T. M. 2020, *Sci*, **368**, eaba3282
- Vigna-Gómez, A., Liu, B., Aguilera-Dena, D. R., et al. 2022, *MNRAS*, **515**, L50
- Vines, J. I., & Jenkins, J. S. 2022, *MNRAS*, **513**, 2719
- Vogt, S. S., Radovan, M., Kibrick, R., et al. 2014, *PASP*, **126**, 359
- Wang, Y., Liao, S., Giacobbo, N., et al. 2022, *A&A*, **665**, A111
- Wiktorowicz, G., Lu, Y., Wyrzykowski, L., et al. 2020, *ApJ*, **905**, 134
- Wiktorowicz, G., Wyrzykowski, L., Chruslinska, M., et al. 2019, *ApJ*, **885**, 1
- Wolf, C., Onken, C. A., Luvaul, L. C., et al. 2018, *PASA*, **35**, e010
- Wright, E. L., Eisenhardt, P. R. M., Mainzer, A. K., et al. 2010, *AJ*, **140**, 1868
- Wright, J. T. 2005, *PASP*, **117**, 657
- Yalinewich, A., Beniamini, P., Hotkezaka, K., & Zhu, W. 2018, *MNRAS*, **481**, 930
- Yamaguchi, M. S., Kawanaka, N., Bulik, T., & Piran, T. 2018, *ApJ*, **861**, 21
- Yee, S. W., Petigura, E. A., & von Braun, K. 2017, *ApJ*, **836**, 77